LYVE-1+ macrophages form a collaborative CCR5-dependent perivascular niche that influences chemotherapy responses in murine breast cancer

Joanne E Anstee, Karen T Feehan, James W Opzoomer, Isaac Dean, Henrike P Muller, Meriem Bahri, Tik Shing Cheung, Kifayathullah Liakath-Ali, Ziyan Liu, Desmond Choy, et al.

Article

Developmental Cell

LYVE-1$^+$ macrophages form a collaborative CCR5-dependent perivascular niche that influences chemotherapy responses in murine breast cancer

Graphical abstract

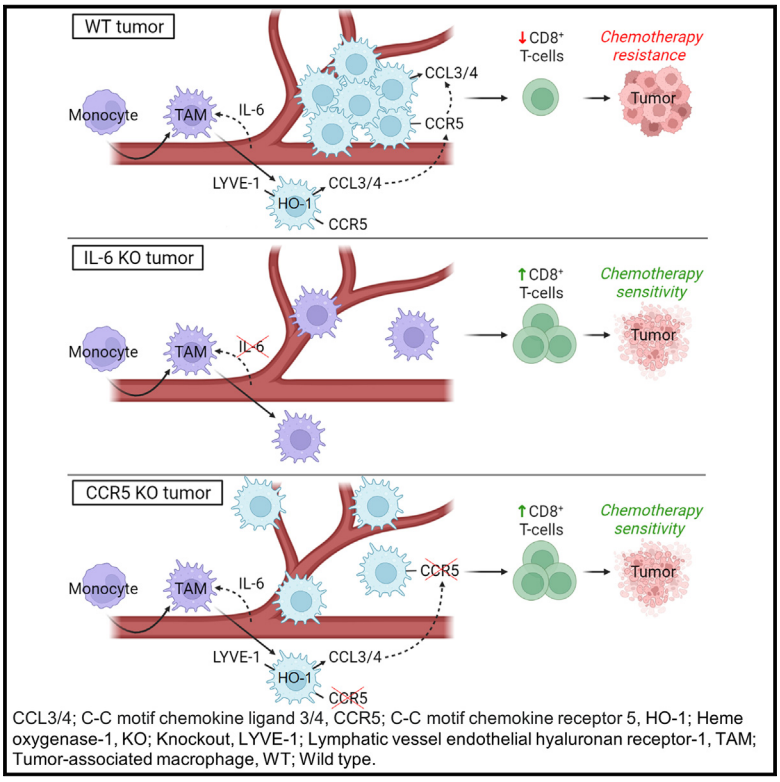

CCL3/4; C-C motif chemokine ligand 3/4, CCR5; C-C motif chemokine receptor 5, HO-1; Heme oxygenase-1, KO; Knockout, LYVE-1; Lymphatic vessel endothelial hyaluronan receptor-1, TAM; Tumor-associated macrophage, WT; Wild type.

Highlights

- LYVE-1$^+$ TAMs co-express HO-1 and form multi-cellular nests proximal to blood vessels
- LYVE-1$^+$ TAMs develop in response to IL-6 within the tumor
- CCR5 drives LYVE-1$^+$ TAMs' cross-communication to form dynamic nest arrangements
- The LYVE-1$^+$ TAM niche facilitates CD8$^+$ T cell exclusion and resistance to chemotherapy

Authors

Joanne E. Anstee, Karen T. Feehan, James W. Opzoomer, ..., David R. Withers, Toby Lawrence, James N. Arnold

Correspondence

james.arnold@kcl.ac.uk

In brief

Lymphatic vessel endothelial hyaluronan receptor-1$^+$ (LYVE-1$^+$) tumor-associated macrophages (TAMs) form coordinated multi-cellular "nests" proximal to blood vasculature in cancer. In a murine breast cancer model, Anstee et al. show that LYVE-1$^+$ TAMs develop in response to IL-6, promoting a CCR5-dependent signaling axis that guides their formation into a collaborative niche.

Anstee et al., 2023, Developmental Cell *58*, 1548–1561
September 11, 2023
https://doi.org/10.1016/j.devcel.2023.06.006

CellPress

CellPress
OPEN ACCESS

Developmental Cell

Article

LYVE-1$^+$ macrophages form a collaborative CCR5-dependent perivascular niche that influences chemotherapy responses in murine breast cancer

Joanne E. Anstee,[1] Karen T. Feehan,[1] James W. Opzoomer,[1,10] Isaac Dean,[2] Henrike P. Muller,[1] Meriem Bahri,[1] Tik Shing Cheung,[1] Kifayathullah Liakath-Ali,[3] Ziyan Liu,[1] Desmond Choy,[1] Jonathan Caron,[1] Dominika Sosnowska,[1] Richard Beatson,[1,11] Tamara Muliaditan,[1,12] Zhengwen An,[1,13] Cheryl E. Gillett,[1] Guocheng Lan,[4,14] Xiangang Zou,[4,15] Fiona M. Watt,[3] Tony Ng,[1,5] Joy M. Burchell,[1] Shahram Kordasti,[1,6] David R. Withers,[2] Toby Lawrence,[7,8,9] and James N. Arnold[1,16,*]

[1]School of Cancer and Pharmaceutical Sciences, King's College London, London SE1 1UL, UK
[2]Institute of Immunology and Immunotherapy, College of Medical and Dental Sciences, University of Birmingham, Birmingham B15 2TT, UK
[3]Centre for Stem Cells and Regenerative Medicine, King's College London, London SE1 9RT, UK
[4]Cancer Research UK Cambridge Research Institute, University of Cambridge, Li Ka Shing Centre, Robinson Way, Cambridge CB2 ORE, UK
[5]UCL Cancer Institute, University College London, London WC1E 6DD, UK
[6]Haematology Department, Guy's Hospital, London SE1 9RT, UK
[7]Centre for Inflammation Biology and Cancer Immunology, School of Immunology & Microbial Sciences, King's College London, London SE1 1UL, UK
[8]Aix Marseille University, CNRS, INSERM, CIML, Marseille, France
[9]Henan Key Laboratory of Immunology and Targeted Therapy, School of Laboratory Medicine, Xinxiang Medical University, Xinxiang, China
[10]Present address: UCL Cancer Institute, University College London, London WC1E 6DD, UK
[11]Present address: Respiratory Medicine, University College London, London WC1E 6JF, UK
[12]Present address: Department of Pharmaceutical Sciences, Faculty of Science, Utrecht University, Utrecht, the Netherlands
[13]Present address: Central Laboratory of Oral Biomedical Research, Dental Institute, Jilin University, Changchun, China
[14]Present address: Stem Cell and Regenerative Consortium Centre, LKS Faculty of Medicine, The School of Biomedical Sciences, The University of Hong Kong, Hong Kong, China
[15]Present address: Chongqing Academy of Animal Science, Rongchang, Chongqing, China
[16]Lead contact
*Correspondence: james.arnold@kcl.ac.uk
https://doi.org/10.1016/j.devcel.2023.06.006

SUMMARY

Tumor-associated macrophages (TAMs) are a heterogeneous population of cells that facilitate cancer progression. However, our knowledge of the niches of individual TAM subsets and their development and function remain incomplete. Here, we describe a population of lymphatic vessel endothelial hyaluronan receptor-1 (LYVE-1)-expressing TAMs, which form coordinated multi-cellular "nest" structures that are heterogeneously distributed proximal to vasculature in tumors of a spontaneous murine model of breast cancer. We demonstrate that LYVE-1$^+$ TAMs develop in response to IL-6, which induces their expression of the immune-suppressive enzyme heme oxygenase-1 and promotes a CCR5-dependent signaling axis, which guides their nest formation. Blocking the development of LYVE-1$^+$ TAMs or their nest structures, using gene-targeted mice, results in an increase in CD8$^+$ T cell recruitment to the tumor and enhanced response to chemotherapy. This study highlights an unappreciated collaboration of a TAM subset to form a coordinated niche linked to immune exclusion and resistance to anti-cancer therapy.

INTRODUCTION

Macrophages are a phenotypically and functionally diverse population of innate immune cells, which become exploited by tumors to facilitate disease progression and therapy resistance.[1–8] Heterogeneity within the tumor-associated macrophage (TAM) population arises from the site of TAM origin[9] and the influence of environmental cues within the tumor microenvironment (TME),[3,10,11] which can be guided by both spatial[12,13] and temporal[11] parameters. This results in the specialization of TAM subsets for executing specific functionality within the TME, which also extends to the co-existence of both pro- and anti-tumoral TAM subsets within the same TME.[14,15] As such, it is vital to understand the respective functionality of TAM subsets and their niches, as optimal TAM-targeted therapeutic strategies could involve the targeting of pro-tumoral TAMs while concurrently preserving and enhancing their anti-tumoral TAM polarization states.

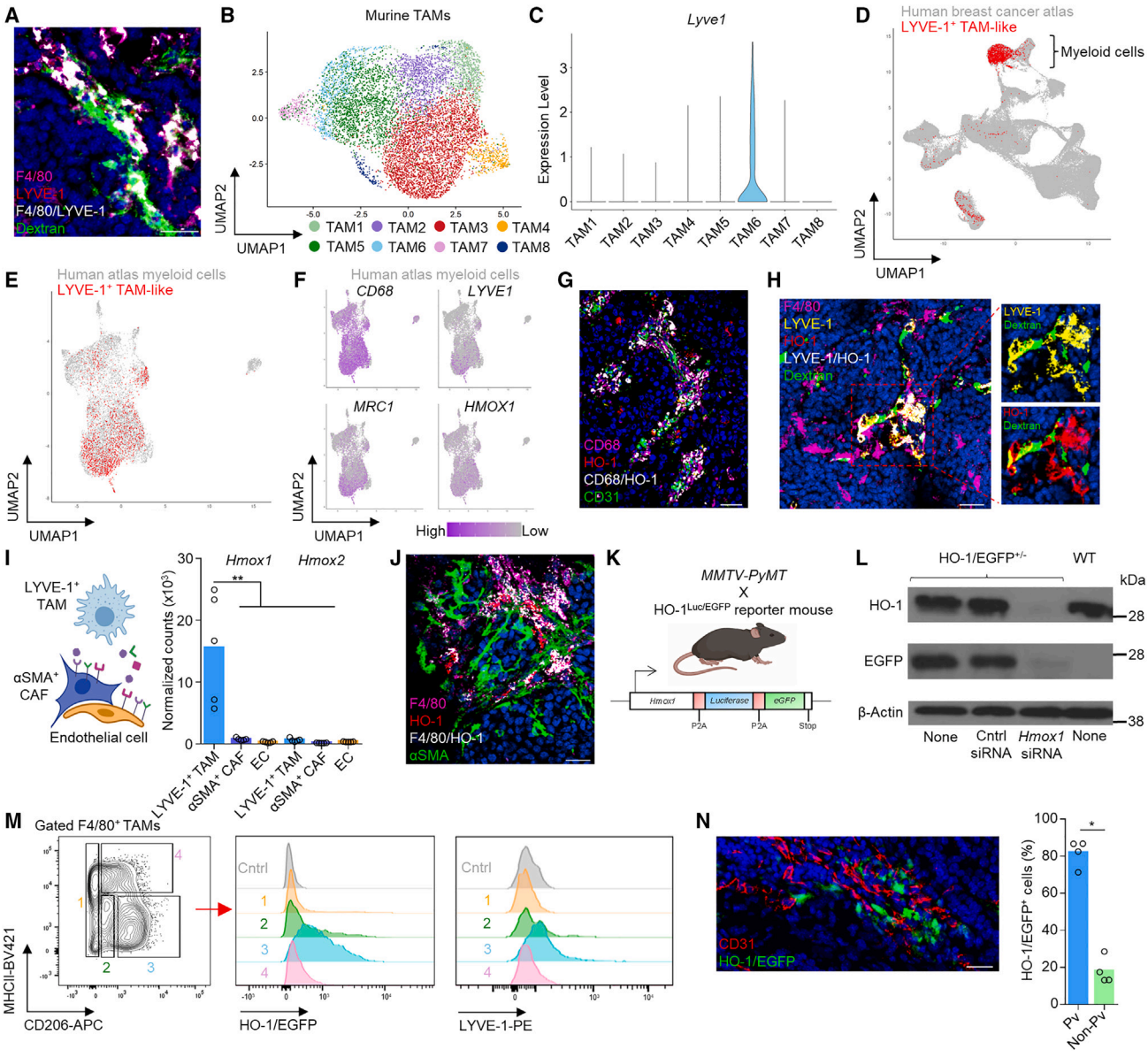

Figure 1. LYVE-1$^+$ macrophages co-express HO-1 and reside in nests within the Pv niche

(A) Representative image of a frozen section of *MMTV-PyMT* tumor stained with DAPI (nuclei;blue) and antibodies against F4/80 (magenta) and LYVE-1 (red). Functional vasculature was labeled *in vivo* using intravenous (i.v.) dextran-fluorescein isothiocyanate (FITC). Colocalizing pixels for F4/80 and LYVE-1 are shown in white. Scale bars: 25 μm.

(B and C) Uniform manifold approximation and projection (UMAP) plot of the scRNA-seq of F4/80$^+$ TAMs from n = 3 *MMTV-PyMT* tumors colored by their associated cluster identity, re-analyzed from Opzoomer et al.[14] (B). Violin plot of Lyve1 expression associated with the TAM cluster identity seen in (C).

(D–F) UMAP plot of scRNA-seq data from a publicly available human breast cancer dataset (gray)[28] identifying cells (red) that were deemed to display a transcriptional phenotype similar to that of the murine LYVE-1$^+$ TAM population,[14] in the full atlas (D) and within the myeloid cluster within the atlas (E). UMAP visualizations of *CD68* and selected genes (*LYVE1*, *MRC1*, and *HMOX1*) (F) that were preferentially expressed ($p < 2.22 \times 10^{-16}$) within the LYVE-1$^+$-like TAM subset compared with other myeloid cells from the human breast cancer dataset.[28]

(G) Representative image of a frozen section of human invasive ductal carcinoma stained with DAPI (nuclei;blue) and antibodies against CD68 (magenta), HO-1 (red), and CD31 (green). Colocalizing pixels for F4/80 and HO-1 are shown in white. Scale bars: 50 μm.

(H) Representative image of a frozen section of *MMTV-PyMT* tumor stained with DAPI (nuclei;blue) and antibodies against F4/80 (magenta), LYVE-1 (yellow), and HO-1 (red). Functional vasculature was labeled *in vivo* using i.v. dextran-FITC. Colocalizing pixels for LYVE-1 and HO-1 are shown in white. Scale bars: 25 μm.

(I) Schematic depicting the cells in the Pv niche (left panel) and their relative expression of *Hmox1* and *Hmox2* from bulk RNA-seq (right panel).

(J) Representative image of a frozen section of *MMTV-PyMT* tumor stained with DAPI (nuclei;blue) and antibodies against F4/80 (magenta), HO-1 (red), and αSMA (green). Colocalizing pixels for F4/80 and HO-1 are shown in white. Scale bars: 25 μm.

(K–N) Schematic depicting the transgene of the HO-1-Luc-EGFP knockin mouse (HO-1$^{Luc/EGFP}$) (lower panel) and the cross that is used in the subsequent tumor studies (upper panel) (K). Western blot of HO-1 and EGFP from BMDMs treated with and without *Hmox1* knockdown (KD) siRNA (n = 3 repeats) (L). Representative

(legend continued on next page)

A collection of TAMs that reside proximal to blood vasculature (<15–20 μm) have emerged as a therapeutic target in cancer,[16,17] as they support a variety of pro-tumoral functions, including neoangiogenesis and[14,17] metastasis,[3,18,19] and facilitate tumor recurrence post chemotherapy.[20] However, they can also elicit immune-stimulatory functions,[15] highlighting the need to further investigate the population and its heterogeneity. We recently characterized a subset of perivascular (Pv) TAMs expressing lymphatic vessel endothelial hyaluronan receptor-1 (LYVE-1$^+$) MHCII^{lo}CD206^{hi}, which orchestrated the expansion of pericyte-like α-smooth muscle actin (α-SMA)-expressing fibroblasts.[14] LYVE-1$^+$ macrophages have been demonstrated to populate a variety of healthy tissues in steady-state conditions[21–25] and accumulate in the TME,[14,15,26,27] however, little is known about their development and function in cancer.[14,15] In this study, we investigate the development of LYVE-1$^+$ TAMs and their Pv niche in *MMTV-PyMT* tumors and define a collaborative function of these cells in forming immune-suppressive multi-cellular "nests," which can influence the response of the tumor to chemotherapy. This study sheds light on the importance of the spatial arrangements of TAMs and their communication axes, which facilitate their pro-tumoral function in cancer.

RESULTS

LYVE-1$^+$ TAMs accumulate in Pv nests within the TME

The LYVE-1$^+$ TAM subset resides in the Pv niche of the TME (Figure 1A). We recently identified LYVE-1$^+$ TAMs from the single-cell RNA sequencing (scRNA-seq) of the F4/80$^+$ TAM population in the *MMTV-PyMT* murine model of breast cancer.[14] To initially investigate whether an analogous TAM population exists in human cancer, we extracted the LYVE-1$^+$ TAM cell cluster as previously described[14] from a scRNA-seq dataset of 9,039 TAMs sorted from 3 individual *MMTV-PyMT* tumors (Figures 1B and 1C). We then mapped the murine LYVE-1$^+$ population onto a recently published scRNA-seq atlas for human breast cancer.[28] The murine LYVE-1$^+$ TAM population identified with cells within the human myeloid cell cluster (Figure 1D; Table S1). Focusing on the myeloid cells within the atlas, 1,444 of the 9,675 myeloid cells were judged to be LYVE-1$^+$ TAM like in their phenotype (Figures 1E and 1F) and their expression of *LYVE1*, *MRC1* (CD206), and *HMOX1* (HO-1) were significantly associated with the identified cells (Figure 1F), demonstrating a conservation of this TAM subset between species. HO-1 is a marker that has previously been associated with PvTAMs in murine models of cancer,[3,20] and the HO-1 expressing TAM population was also observed in the Pv niche of human cancer (Figure 1G), highlighting a similar spatial location for these cells between species. HO-1 and LYVE-1 protein co-localized in tumor sections from *MMTV-PyMT* mice (Figure 1H), and LYVE-1$^+$ TAMs were the major source of HO-1 within the Pv niche, which also includes, endothelial cells (ECs) and pericyte-like αSMA-expressing cancer-associated fibroblasts (CAFs) (Figures 1I and 1J).[14] Interestingly, from these analyses, it was evident that the LYVE-1$^+$HO-1$^+$ PvTAM subset was heterogeneously distributed along the endothelium and clustered to discrete regions where these cells were either lining or appearing in bunches proximal to the vasculature (Figures 1A, 1G, 1H, 1J, and S1A). These clusters, which we herein refer to as nests, highlighted an unappreciated multi-cellular PvTAM structure within the TME. As LYVE-1 is also expressed at high levels by the lymphatic endothelium,[29] and HO-1 expression is selectively expressed by this TAM subset (Figures 1H–1J), we generated a knockin reporter mouse for the *Hmox1* gene to facilitate the study of these cells (Figure 1K). The reporter consisted of Click Beetle luciferase (Luc) and enhanced green fluorescent protein (EGFP)[30] inserted before the stop codon of the genomic *Hmox1* gene locus. HO-1, Luc, and EGFP were separated by a self-cleaving P2A sequence[31] to allow the equimolar expression of the three proteins (Figures 1K, 1L, and S1B) (mouse herein referred to as HO-1$^{Luc/EGFP}$). As HO-1 plays several important functional roles in the TME,[3,32–34] the arrangement of the reporter construct ensured that native HO-1 expression was unaffected by the reporter elements. In HO-1$^{Luc/EGFP}$ mice, HO-1 expression could be detected in healthy tissues using bioluminescence imaging (Figure S1C). Analysis of healthy tissues from the HO-1$^{Luc/EGFP}$ mouse revealed the spleen, lung, mammary gland, visceral adipose, skin, and liver to be among the highest expressing tissues for HO-1 (Figure S1D), where its expression was restricted to F4/80^{hi}-tissue-resident macrophages (Figure S1E). The HO-1$^{Luc/EGFP}$ mouse was crossed onto the *MMTV-PyMT* background, and tumors were analyzed for their distribution of HO-1/EGFP expression (Figure 1K). TAMs (Figure S1F), specifically the LYVE-1$^+$CD206^{hi}MHCII^{lo} TAM subset (Figures 1M and S1G), were the major tumoral source of HO-1/EGFP. Further characterization of F4/80$^+$HO-1/EGFP$^+$ cells in tumors by immunofluorescence analysis also confirmed the localization of HO-1/EGFP to the Pv space within nest structures (Figure 1N). These data validate the HO-1$^{Luc/EGFP}$-reporter mouse as a tool for studying LYVE-1$^+$ PvTAMs and identify a previously unappreciated multicellular nest structure for these cells in the Pv space.

LYVE-1$^+$ TAMs develop in the TME in response to IL-6

To investigate the development of LYVE-1$^+$ TAMs within TME, we first considered whether they were a recruited or tissue-resident TAM population.[9] To address this question, we utilized the photoconvertible *Kaede* mouse[35] crossed to the *MMTV-PyMT* model. When tumors reached 100 mm^3, the entire TME was photoconverted from *Kaede*-green to *Kaede*-red using a UV-light source (Figure 2A). After 48 h post photoconversion of the TME, there was a clear *Kaede*-green (-red-negative) population of LYVE-1$^+$ TAMs in the TME, indicative of their development from a recruited progenitor cell originating from outside the TME (Figure 2B). Although it is possible that highly replicating

contour plot of fluorescence-activated cell sorting (FACs)-gated live (7AAD$^-$) CD45$^+$F4/80$^+$ TAMs from enzyme-dispersed *MMTV-PyMT* HO-1$^{Luc/EGFP}$ tumors separated based on their respective expression of CD206 and MHCII (left panel) and then assessed for their expression of HO-1 and LYVE-1 (right panel; colored histograms) against that of the FMO staining control (gray histogram) (M). Representative of n = 10 mice. Representative image of a frozen section and quantification of a *MMTV-PyMT* HO-1$^{Luc/EGFP}$ tumor stained with antibodies against CD31 (red) are shown, and native EGFP fluorescence is shown in green (N). Scale bars: 25 μm (left panel). Proportion of HO-1/EGFP$^+$ cells that are Pv (<20 μm from live vasculature) across n = 4 *MMTV-PyMT* tumors (right panel). Images in (I) and (K) were created using *BioRender* software. Bar charts represent the mean, and the dots show individual data points from individual tumors and mice. * $p < 0.05$, ** $p < 0.01$.

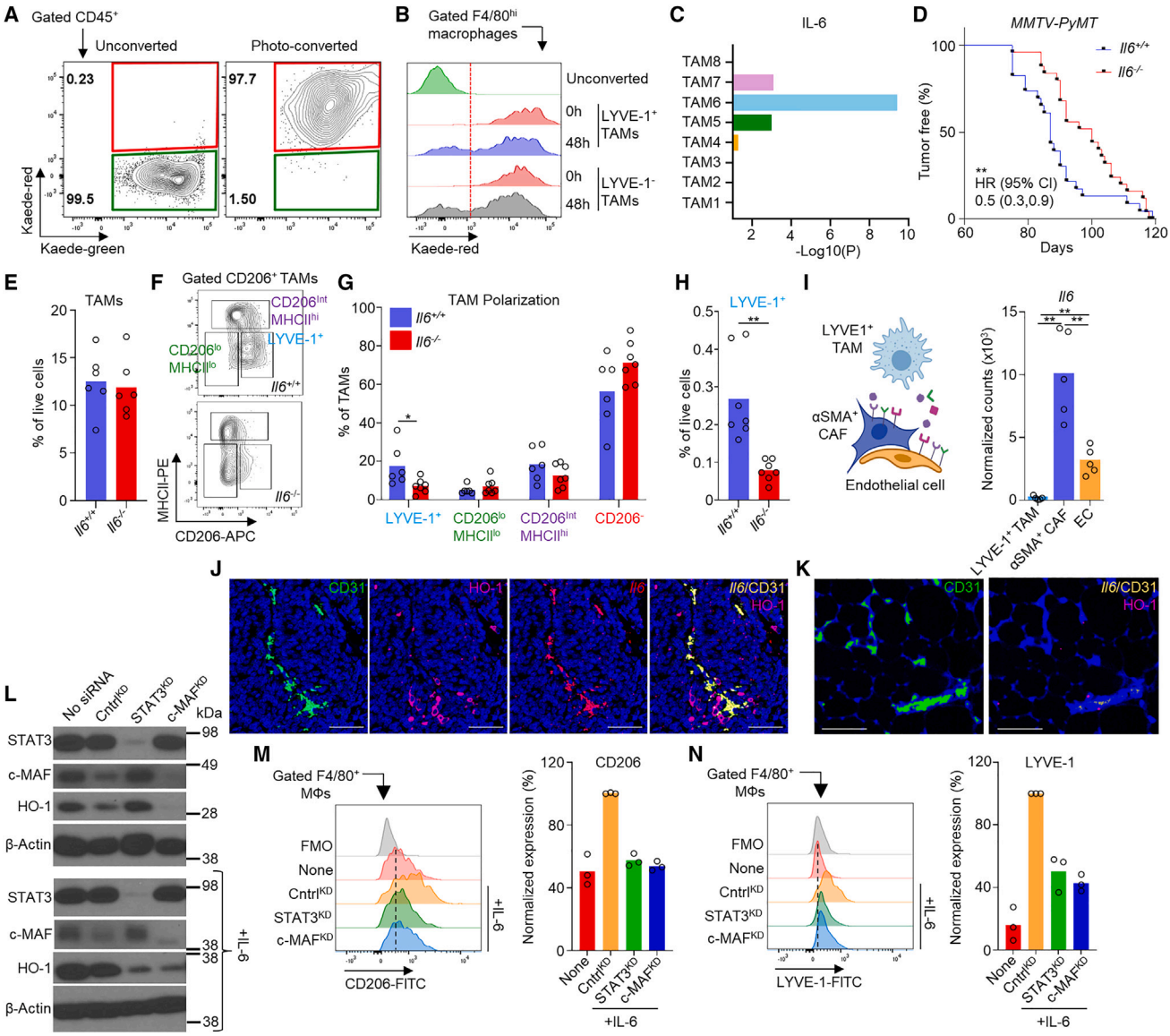

Figure 2. LYVE-1$^+$ PvTAMs are polarized by IL-6 in the tumor

(A and B) Established tumors in *MMTV-PyMT Kaede* mice were photoconverted to *Kaede*-red (A). After 48 h, photoconverted tumors were analyzed for *Kaede*-red using flow cytometry, where cells negative for *Kaede*-red represent recruitment from outside the TME (B).

(C) Plot showing the significance value of IL-6 as a predicted upstream regulator of the gene expression profile of the respective TAM populations identified in Figure 1B generated by the IPA regulator analytic.

(D) Kaplan-Meier curve showing the tumor latency period for *Il6*$^{+/+}$ (WT; n = 23) and *Il6*$^{-/-}$ (n = 25) *MMTV-PyMT* mice; HR, hazard ratio; exact significance p = 0.0062.

(E–H) Abundance of live (7AAD$^-$) CD45$^+$F4/80$^+$Ly6C$^-$ TAMs in enzyme-dispersed tumors from *Il6*$^{+/+}$ and *Il6*$^{-/-}$ *MMTV-PyMT* mice assessed using flow cytometry (n = 6 per group) (E). Representative contour plot of FACs-gated live (7AAD$^-$) F4/80$^+$CD206$^+$ TAMs from enzyme-dispersed *MMTV-PyMT* tumors showing their respective expression of CD206 and MHCII in *Il6*$^{+/+}$ (upper panel) and *Il6*$^{-/-}$ (lower panel) mice (F) and the quantification of the respective TAM populations (G) and abundance of LYVE-1$^+$ TAMs as percentage of live cells (H) (n = 7 per group).

(I) Schematic depicting the cells in the Pv niche (left panel) and their relative expression of *Il6* mRNA from bulk RNA-seq (right panel).

(J and K) Representative images of formalin-fixed paraffin-embedded (FFPE) sections of *MMTV-PyMT* tumor (J) and healthy mammary gland (K) stained with DAPI (nuclei;blue) and antibodies against CD31 (green) and HO-1 (magenta) and probed for *Il6* mRNA (red). Co-localization of *Il6* and CD31 is displayed in yellow. Scale bars: 25 μm.

(L–N) BMDMs treated with and without IL-6 and the indicated knockdown (KD) siRNAs (n = 3 repeats). Western blots probing for STAT3 and c-MAF in cell lysates (L). Representative histograms of surface CD206 (left panel) and normalized (to Cntrl^{KD}) marker expression across three individual experiments (right panel) (M) and representative histograms of surface LYVE-1 (left panel) and normalized (to Cntrl^{KD}) marker expression across three individual experiments (right panel) (N); expression was assessed using a flow cytometry of BMDMs.

Image in (I) was created using *BioRender* software. Bar charts represent the mean, and the dots show individual data points from individual tumors and mice. * p < 0.05, ** p < 0.01.

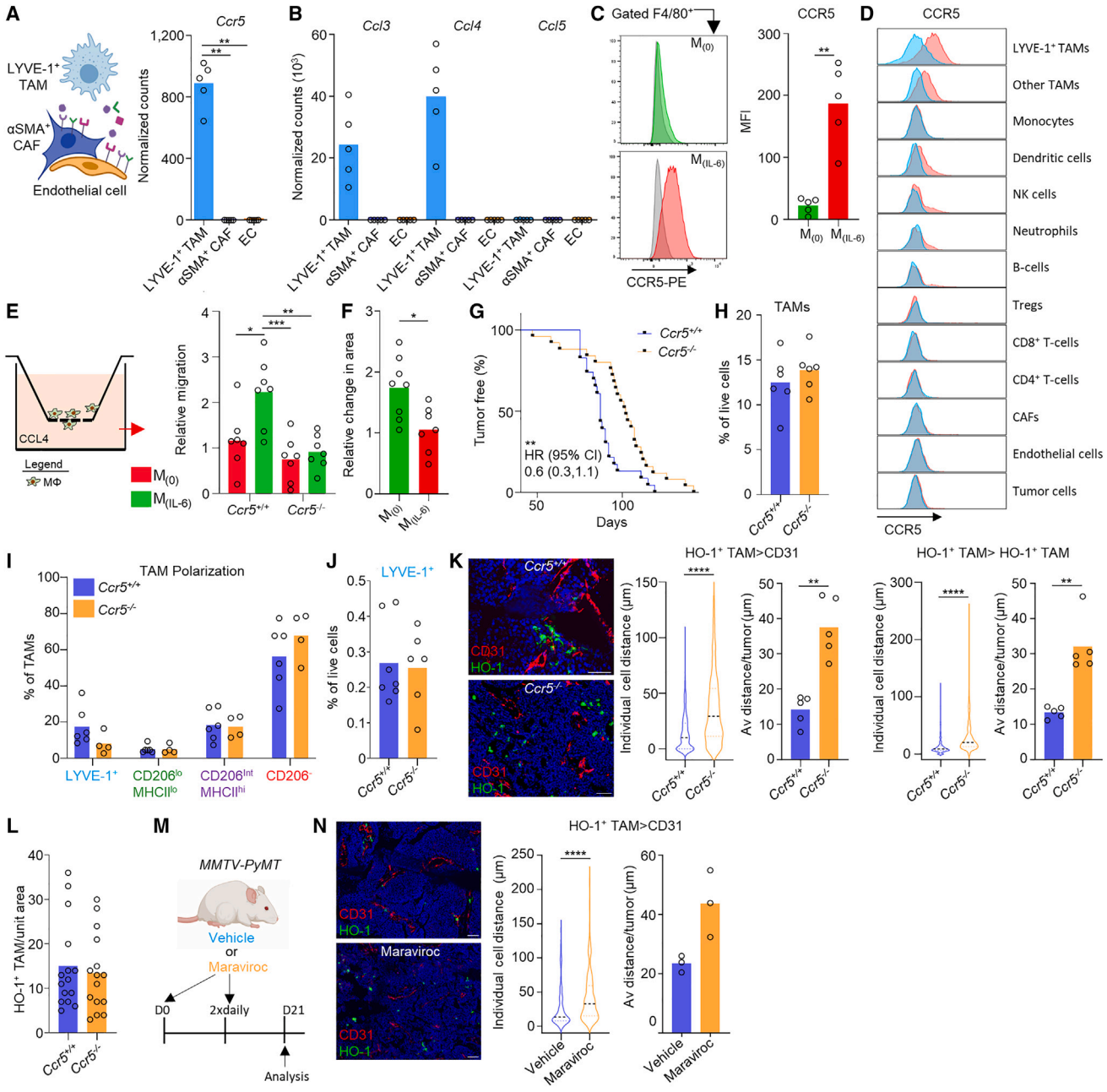

Figure 3. LYVE-1⁺ TAMs communicate via a CCR5-dependent axis to maintain Pv nest formation

(A and B) Schematic overview of cells in the Pv nest (A, left) and bar plot depicting normalized gene expression values for *Ccr5* in the bulk RNA-seq of the Pv niche populations (A, right) and *Ccl3*, *Ccl4*, and *Ccl5* (B) across n = 5 mice.

(C) Representative histograms of surface CCR5 expression in BMDMs treated with (red-filled histogram lower panel) and without (green-filled histogram upper panel) IL-6 against that of FMO staining (gray-filled histogram) (left) and quantitation of CCR5 expression (median fluorescence intensity [MFI]-subtracted FMO) across 5 biological repeats (right).

(D) Representative histograms of surface CCR5 expression (red histogram) for the indicated populations against that of the fluorescence minus one (FMO) staining control (blue histogram) in enzyme-dispersed *MMTV-PyMT* HO-1$^{Luc/EGFP}$ tumors where the Lyve-1⁺ TAM population was gated based upon their GFP/HO-1 expression.

(E) Schematic of the assay (left panel) and relative transendothelial migration (TEM) of $M_{(0)}$ and $M_{(IL-6)}$ BMDMs generated from *Ccr5*$^{+/+}$ and *Ccr5*$^{-/-}$ mice in the presence or absence of CCL4 after 24 h incubation (right panel). Each dot represents a paired ratio of CCL4/control (no CCL4) (n = 7).

(F) Relative change in the area of plated $M_{(0)}$ and $M_{(IL-6)}$ BMDMs spheroids over 72 h. Each point represents an individual spheroid.

(G) Kaplan-Meier curve showing the tumor latency for *Ccr5*$^{+/+}$ (WT; n = 23) and *Ccr5*$^{-/-}$ (n = 25) *MMTV-PyMT* mice; HR, hazard ratio; exact significance p = 0.004.

(H–J) Tumors from *Ccr5*$^{+/+}$ and *Ccr5*$^{-/-}$ *MMTV-PyMT* mice were enzyme dispersed and assessed using flow cytometry for the abundance of live (7AAD⁻) CD45⁺F4/80⁺Ly6C⁻ TAMs (H) and their phenotype as proportions of the TAM gate (I) and the abundance of LYVE-1⁺ TAMs as the percentage of live cells (J) (n = 4–7 per group).

(legend continued on next page)

cells can dilute their *Kaede*-red status post photoconversion, an analysis of the expression of the proliferation marker Ki-67 revealed that 40% ± 20% of the *Kaede*-green-gated LYVE-1$^+$ TAMs did not express Ki-67. This highlights that a significant proportion of these cells were not replicating (Figures S2A and S2B). Furthermore, there was no difference in Ki-67 expression between *Kaede*-red and *Kaede*-green LYVE-1$^+$ TAMs (Figures S2A and S2B). As such, these data suggest recruitment as the most likely origin of these cells. As LYVE-1$^+$ TAMs were likely developing and polarizing within the TME, to explore the key signals directing this developmental program, we employed the QIAGEN Ingenuity Pathway Analysis software (QIAGEN IPA)[36] on a scRNA-seq data of TAMs from *MMTV-PyMT* tumors.[14] Using this approach, IL-6 signaling was predicted to be an upstream polarization signal associated with the transcriptional programs active in the LYVE-1$^+$ TAM subset (Figure 2C). To investigate the role of IL-6 in the polarization of the LYVE-1$^+$ PvTAM subset, we crossed *MMTV-PyMT* mice onto an *Il6*$^{-/-}$ background and analyzed the tumors in these animals. In the absence of IL-6, the tumors were significantly slower to establish, with a median latency of 87 versus 100 days for *Il6*$^{+/+}$ and *Il6*$^{-/-}$ *MMTV-PyMT* mice, respectively (Figure 2D). When tumors reached ~500 mm^3, they were enzyme dispersed and analyzed by flow cytometry. Despite no overall change in the abundance of TAMs within the TME (Figure 2E), there was a significant and selective loss of the LYVE-1$^+$ TAM subset (Figures 2F–2H), highlighting that IL-6 was fundamental to the polarization of the TAM subset. Analysis of bulk RNA-seq data from sorted TME stromal populations within the Pv niche[14] highlighted the αSMA$^+$ pericyte-like CAF and ECs (but not the TAMs) to express *Il6* mRNA (Figure 2I). More widely, CAFs and ECs were the main tumoral sources of *Il6* mRNA expression, with no detectable expression in the tumor cells or other stroma subsets (Figure S2C). To identify the spatial location of the *Il6* mRNA in the TME, we used RNAscope (Figure 2J). *Il6* mRNA was detectable in nearly all ECs in the tumor, but the highest expression of *Il6* mRNA was evident in the ECs that were proximal to HO-1$^+$ cells (LYVE-1$^+$ TAMs) (Figures 2J and S2D–S2F); although αSMA$^+$ CAFs could be found expressing *Il6* mRNA in the TME, as indicated by the bulk RNA-seq data, the cells expressing *Il6* mRNA were not proximal to the HO-1$^+$ cells (Figures S2D and S2E). Interestingly, *Il6* was not expressed by the endothelium, nor were HO-1$^+$ macrophage clusters present in the healthy mammary gland (Figure 2K), highlighting this axis to be associated specifically with the TME. These data suggest that LYVE-1$^+$ TAMs develop within the Pv niche in response to IL-6 and that the proximal endothelium is the most likely source of IL-6 in the TME.

LYVE-1$^+$ macrophage phenotypic identity is dependent on STAT3/c-MAF pathways

To investigate whether IL-6 stimulation alone was sufficient to generate a LYVE-1$^+$ TAM-like phenotype, in a gain-of-function experiment, bone-marrow-derived macrophages (BMDMs) were exposed to IL-6, and their phenotype was assessed. IL-6-stimulated BMDMs upregulated the expression of the three key phenotypic markers, HO-1 (Figures 2L, S2G, and S2H), CD206 (Figure 2M), and LYVE-1 (Figure 2N), which define the subset. These data suggested that IL-6 plays a dominant role in the polarization identity of LYVE-1$^+$ TAMs, and the relative absence of the LYVE-1$^+$ macrophage phenotype in *Il6*$^{-/-}$ *MMTV-PyMT* mice (Figures 2F–2H) was most likely directly due to the loss of IL-6 from the TME. Recent data demonstrated that the transcription factor cellular musculoaponeurotic fibrosarcoma (c-MAF) was vital to the development of LYVE-1$^+$ Pv macrophages in healthy tissues,[37] and we sought to establish whether c-MAF signaling may account for the LYVE-1$^+$ macrophage phenotype observed through IL-6 stimulation. IL-6 signaling is associated with the Janus kinase (JAK)/signal transducer and activator of transcription protein-3 (STAT3) pathway[38]; however, STAT3 has been linked to the expression of c-MAF via the basic leucine zipper transcription factor activating transcription factor (ATF)-like Batf in T follicular helper cells.[39] To investigate whether c-MAF and STAT3 signaling play a role in the LYVE-1$^+$ macrophage phenotype, we knocked down the expression of either c-MAF or STAT3 in BMDMs prior to stimulation by IL-6 (Figures 2L and S2G). Loss of either transcription factor in IL-6 stimulated BMDMs, indeed, compromised the phenotypic identity of the population, as assessed using the markers LYVE-1, CD206, and HO-1 (Figures 2L–2N and S2H). Interestingly, c-MAF appeared to be required for even basal HO-1 expression in BMDMs (Figures 2L and S2H). These data demonstrate that IL-6 is sufficient to upregulate the key phenotypic markers associated with the LYVE-1$^+$ PvTAM subset through a STAT3- and c-MAF-dependent pathway.

LYVE-1$^+$ TAMs communicate via a CCR5-dependent axis to maintain nest formation

Having identified IL-6 as a driver of the LYVE-1$^+$ TAM polarization program in the Pv niche (Figure 2), we investigated whether the polarization program might influence a communication axis between these cells required to maintain the formation of nests arrangements post polarization (Figure 1A). As such, to screen for IL-6-regulated chemokine receptors within the polarization program, we performed a microarray analysis on

(K and L) Representative images of a frozen section of *MMTV-PyMT* tumor stained with DAPI (nuclei;blue) and antibodies against CD31 (red) and HO-1 (green) in *Ccr5*$^{+/+}$ (K, upper left) and *Ccr5*$^{-/-}$ (K, lower left) *MMTV-PyMT* mice. Scale bars: 50 μm (left panel). Distance of individual HO-1$^+$ TAMs to the nearest CD31$^+$ cell or HO-1$^+$ TAM as indicated, plotting individual cells (left panels, taken across 3 sections from each tumor and an average of 145 ± 65 and 175 ± 72 measurements per tumor between CCR5$^{+/+}$ and CCR5$^{-/-}$ groups, respectively) and average distances per tumor (right panels). Also plotted is the abundance of HO-1$^+$ TAMs per unit area (L) in *Ccr5*$^{+/+}$ and *Ccr5*$^{-/-}$ *MMTV-PyMT* tumors (taken from n = 5 tumors).

(M and N) Schematic representing the dosing strategy for the CCR5 inhibitor maraviroc and vehicle in *MMTV-PyMT* mice (n = 3 per group) (M). Representative images of a frozen section of *MMTV-PyMT* tumor stained with DAPI (nuclei;blue) and antibodies against CD31 (red) and HO-1 (green) in vehicle-treated mice (N, upper left) and maraviroc-treated mice (N, lower left). Scale bars: 50 μm (left panel). Distance of individual HO-1$^+$ TAMs to nearest CD31$^+$ cell across vehicle- and maraviroc-treated *MMTV-PyMT* tumors, plotting individual cells (left panel, taken across 3 sections from each tumor and an average of 71 ±36 and 128 ±12 measurements per tumor between vehicle- and maraviroc-treated groups, respectively) and average distances per tumor (right panel) (N). Images in (A) and (M) were created using *BioRender* software. Bar charts represent the mean, and the dots show individual data points from individual tumors and mice. * $p < 0.05$, ** $p < 0.01$, and ****$p < 0.0001$.

monocyte-derived macrophages exposed to IL-6, using basal (M0), IL-4 (M2), and IFNγ/lipopolysaccharide (LPS) (M1)[40] as comparator conditions (Figures S3A and S3B). The IL-6 polarization program was a distinct program from that of M1/M2 macrophages (Figures S3A and S3B). Interestingly, IL-6-polarized macrophages ($M_{(IL-6)}$) were associated with higher *Pdgfc* expression (Figure S3C), a growth factor we recently demonstrated to play a role in the LYVE-1$^+$ TAM-dependent expansion of αSMA CAFs within the Pv niche.[14] In probing for IL-6-induced chemokine receptors, we identified a unique upregulation of the chemokine receptor gene *Ccr5* (Figure S3D). Analyzing the bulk RNA-seq data for cells in the Pv niche revealed both *Ccr5* (Figure 3A) and its cognate ligands *Ccl3* and *Ccl4* (Figure 3B) to be expressed by the LYVE-1$^+$ TAMs within the Pv niche and identified a potential communication axis for these cells post IL-6 polarization. The expression of CCR5 was also regulated by IL-6 in BMDMs (Figure 3C), implicating the gene within the IL-6 polarization program. Within the TME, although all TAMs expressed some CCR5, the LYVE-1$^+$ TAM subset was the highest expressor (Figures 3D and S3E). CCR5 was functional on the macrophages, and IL-6-stimulated BMDMs could migrate toward the CCR5 ligand, CCL4 (Figure 3E). Chemotaxis to CCL4 was CCR5 dependent, as migration was abolished when IL-6-stimulated BMDMs were derived from *Ccr5*$^{-/-}$ mice (Figure 3E). When IL-6-stimulated BMDMs were also placed in close contact *in vitro*, their ability to spread from one another was also reduced (Figure 3F). To test the role of CCR5 in maintaining LYVE-1$^+$ TAMs in nests within the TME, we crossed *MMTV-PyMT* mice onto a *Ccr5*$^{-/-}$ background. In the absence of CCR5, tumors were significantly slower to establish, with a median latency of 87 versus 102 days for *Ccr5*$^{+/+}$ and *Ccr5*$^{-/-}$ *MMTV-PyMT* mice, respectively (Figure 3G). The loss of CCR5 did not affect the total prevalence of TAMs (Figure 3H) or the LYVE-1$^+$ TAM subset (Figures 3I and 3J) in these tumors, demonstrating that CCR5 expression was not required for the maintenance of the polarization phenotype of these cells. However, immunofluorescence imaging of tissue sections from these tumors revealed an increase in the median distance between LYVE-1$^+$ TAMs and from LYVE-1$^+$ TAMs to the endothelium (Figure 3K), with no effect on their abundance overall (Figure 3L). This demonstrated that CCR5 was required to maintain the formation of the nest structures of LYVE-1$^+$ TAMs and is a key functional protein of the IL-6 polarization program that spatially orientates these cells within the Pv niche. To explore whether the Pv niche was a dynamic structure and whether CCR5 also played an ongoing active role in maintaining the LYVE-1$^+$ TAM nests post formation, rather than just the initial formation of the structure, we injected *MMTV-PyMT* mice with maraviroc (Figure 3M), a drug that is clinically used to inhibit CCR5.[41] Therapeutically blocking CCR5 signaling using maraviroc in tumors with pre-formed LYVE-1$^+$ PvTAM nests (Figures S3F and S3G) resulted in an observable dispersion of the LYVE-1$^+$ TAM nests away from the Pv space (Figure 3N), highlighting that LYVE-1$^+$ TAM nests are, indeed, dynamic structures and that CCR5 represents an ongoing communication axis for their maintenance. These data highlight a role for CCR5 in the collaborative formation and maintenance of the LYVE-1$^+$ TAM nests that create a Pv niche.

LYVE-1$^+$ TAM nests are associated with immune exclusion in the TME

To understand how the absence of LYVE-1$^+$ TAM nests may alter the wider TME, we analyzed the composition of the stroma in ~500 mm^3 tumors from wild type (WT), *Il6*$^{-/-}$ (where LYVE-1$^+$ TAMs could not develop), and *Ccr5*$^{-/-}$ (where their post-IL-6 polarization nesting was perturbed) *MMTV-PyMT* mice (Figure 4A). The stromal composition in enzyme-dispersed tumors were assessed using flow cytometry (Figures 4B and S4A). Broadly, the stromal composition of the tumors was highly similar despite the spontaneous nature of the tumor model (Figure 4B). However, the only consistent difference between both the *Il6*$^{-/-}$ and *Ccr5*$^{-/-}$ *MMTV-PyMT* mice and WT mice was a significant increase in tumor-infiltrating CD8$^+$ T cells (Figure 4B). The CD8$^+$ T cells had a similar overall proportion of cells that displayed effector function (Figures 4C, 4D, and S4B). The increase in tumor-infiltrating CD8$^+$ T cells observed in the tumors from *Il6*$^{-/-}$ and *Ccr5*$^{-/-}$ *MMTV-PyMT* mice appeared independent from a change in the vasculature, as all tumors had equivalent numbers of CD31$^+$ ECs (Figure 4B) and an equivalent vessel density in the tissue (Figure 4E). The endothelium expresses adhesion molecules, which permit leukocyte rolling, migration, and arrest prior to diapedesis into inflamed tissues,[42] and it was possible that LYVE-1$^+$ TAMs could modulate the endothelium due to their close proximity to one another. However, there was no evidence for a change in the expression of endothelial VCAM-1, ICAM-1, or PNAd in the absence of LYVE-1$^+$ TAMs or their nests in the TME (Figure S5A). However, this highlighted that the key signaling axes, which are required for the polarization (IL-6) and spatial identity (CCR5) of LYVE-1$^+$ TAMs, were associated with immune exclusion within the TME and were independent of the pro-angiogenic function of these cells.

Loss of LYVE-1$^+$ TAMs or their nests improves the immune-mediated effects of chemotherapy

There is a clear clinical link between the presence of tumor-infiltrating lymphocytes (TILs) and response to therapeutics that can modulate their effects through anti-tumor immune responses, such as immune checkpoint blockade[43,44] and cytotoxic chemotherapies.[45,46] We have demonstrated HO-1 activity to be a major immune-suppressive pathway preventing chemotherapy-elicited immune responses in the TME.[47] In this study, we have demonstrated that HO-1 expression is highly restricted to the LYVE-1$^+$ TAM population (Figure 1). As such, we considered whether the presence of LYVE-1$^+$ TAMs, or their nest structures, might influence the resistance to immune-modulating cytotoxic chemotherapeutics. Treatment of tumor-bearing *MMTV-PyMT* mice with 5-fluorouracil (5-FU), a chemotherapeutic that has been used in the clinic[48] and that has been demonstrated to have immune-stimulatory capabilities,[49,50] did not significantly affect tumor growth in WT mice (Figures 4F and 4G). However, when 5-FU was administered to either *Il6*$^{-/-}$ or *Ccr5*$^{-/-}$ mice, a significant control of tumor growth was achieved (Figure 4G). To investigate whether the tumor control was immune dependent, we depleted CD8$^+$ T cells using immune-depleting antibodies *in vivo* prior to the initiation of 5-FU treatment in *Il6*$^{-/-}$ and *Ccr5*$^{-/-}$ *MMTV-PyMT* mice in which the LYVE-1$^+$ TAM subset was unable to polarize (*Il6*$^{-/-}$) or form Pv nest structures (*Ccr5*$^{-/-}$) (Figures S5B–S5D). In the absence of CD8$^+$ T cells,

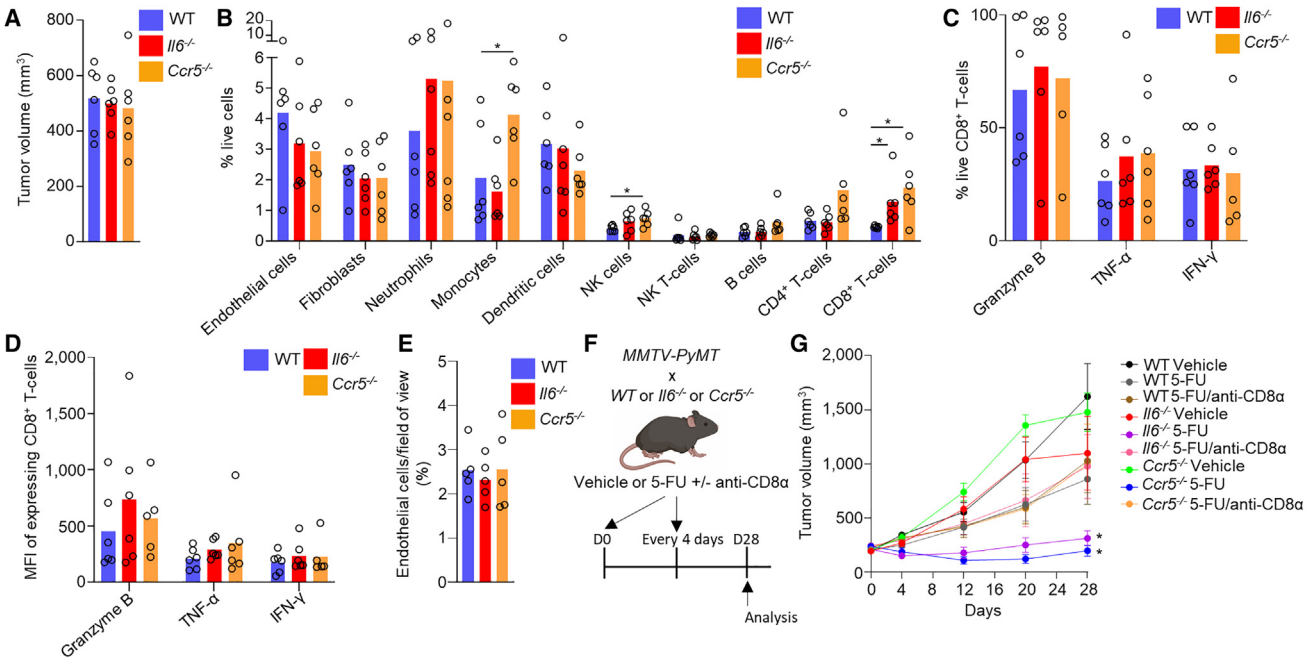

Figure 4. LYVE-1$^+$ TAMs and their nests are associated with immune exclusion and resistance to chemotherapy

(A–E) Tumors from WT, *Il6*$^{-/-}$, or *Ccr5*$^{-/-}$ *MMTV-PyMT* mice were analyzed for their stromal composition (n = 6 tumors per group). Tumor sizes on the day of analysis (A) and the relative proportions of live (7AAD$^-$) stromal cell populations were assessed using flow cytometry (B). The markers used to differentiate cells can be found in the online STAR Methods. Gated CD8$^+$CD3$^+$ T cells were assessed for their expression of the indicated effector molecules post PMA/ionomycin treatment, shown as percentage of positive cells (C), and the MFI of the expression of the gated positive cells (D). CD31$^+$ cell density was assessed in tumor sections by immunofluorescence and quantitated relative to DAPI staining (taken from multiple images from n = 5 tumors per group) (E).

(F and G) Schematic representing the dosing strategy for 5-FU and/or immune-depleting anti-CD8α antibodies in *MMTV-PyMT* mice. When mice received anti-CD8α antibodies, they were also given a day-2 loading dose, which is not depicted on the schematic (F). Growth curves of established spontaneous tumors in WT, *Il6*$^{-/-}$, and *Ccr5*$^{-/-}$ *MMTV-PyMT* mice that were given 5-FU (40 mg/kg/4 days) or their respective vehicles and immune-depleting anti-CD8α IgG where indicated (G). Indicated dosing started at day 0 (cohorts of n = 4–9 mice).

Image in (F) was created using *BioRender* software. Bar charts show the mean, and the dots show individual data points from individual tumors and mice. Line charts display the mean and SEM. * $p < 0.05$.

5-FU had no effect on tumor growth in *Il6*$^{-/-}$ or *Ccr5*$^{-/-}$ tumors (Figures 4F and 4G), demonstrating that CD8$^+$ T cells were directly implicated in the mechanism of tumor control observed in response to chemotherapy. As such, these data highlight an intriguing association between the LYVE-1$^+$ PvTAM niche and the immune landscape of the TME, which can provide a resistance mechanism for the immune-mediated effects of cytotoxic chemotherapeutics.

LYVE-1$^+$ macrophages suppress CD8$^+$ T cell transendothelial migration

To investigate whether LYVE-1$^+$ TAMs may be playing a direct role in immune exclusion within the TME, we established an *in vitro* assay for creating artificial Pv nests (Figure 5A). In this assay, $M_{(IL\text{-}6)}$, which are analogous to the LYVE-1$^+$ TAMs (Figures 2L, 2M and 2N), were seeded onto the basolateral side of a transwell insert, and then a basement membrane and an endothelial layer were seeded on the apical side of the insert (Figure 5A). The presence of $M_{(0)}$ or $M_{(IL6)}$ on the apical side did not change the permeability or integrity of the endothelial layer (Figure 5B). However, when CD8$^+$ T cells were placed in contact with the endothelial layer with a gradient of the T cell chemokine CXCL10, there was a significant reduction in T cell migration across the endothelial layer in the presence of $M_{(IL6)}$ (Figure 5C). HO-1 is an enzyme that breaks down heme into the biologically active catabolites biliverdin, ferrous iron (Fe^{2+}), and carbon monoxide (CO), and its activity has been demonstrated to play a role in vascular biology.[33,51] As such, we considered whether the enzyme might play a direct role in the mechanism of CD8$^+$ T cell exclusion. Inactivation of the *Hmox1* gene in the $M_{(IL\text{-}6)}$ BMDMs (Figure S5E) improved T cell transendothelial migration in the *in vitro* assay (Figure 5D). These data suggest that HO-1 activity, at least in part, contributed to the mechanism of T cell exclusion by $M_{(IL\text{-}6)}$ macrophages.

To investigate whether HO-1 expression by LYVE-1$^+$ TAMs played a direct role in the immune exclusion within the PV niche, we crossed *MMTV-PyMT* to a *Hmox1*$^{fl/fl}$ background with and without a *Lyve1*-promoter-driven Cre-recombinase (referred to as *Lyve1*^{Cre} or *Lyve1*^{WT} mice, respectively) to inactivate the HO-1 protein in the TAM subset (Figures 5E and S5F). Inactivation of HO-1 selectively in the LYVE-1$^+$ TAM population resulted in a non-significant change in tumor latency, with a median latency of 104 versus 108 days for *Lyve1*^{WT} and *Lyve1*^{Cre} mice, respectively (Figure 5F). At the cellular level within the TME, the loss of HO-1 activity in this TAM subset did not affect the total prevalence of TAMs (Figure 5G) or the TAM subsets (Figures 5H

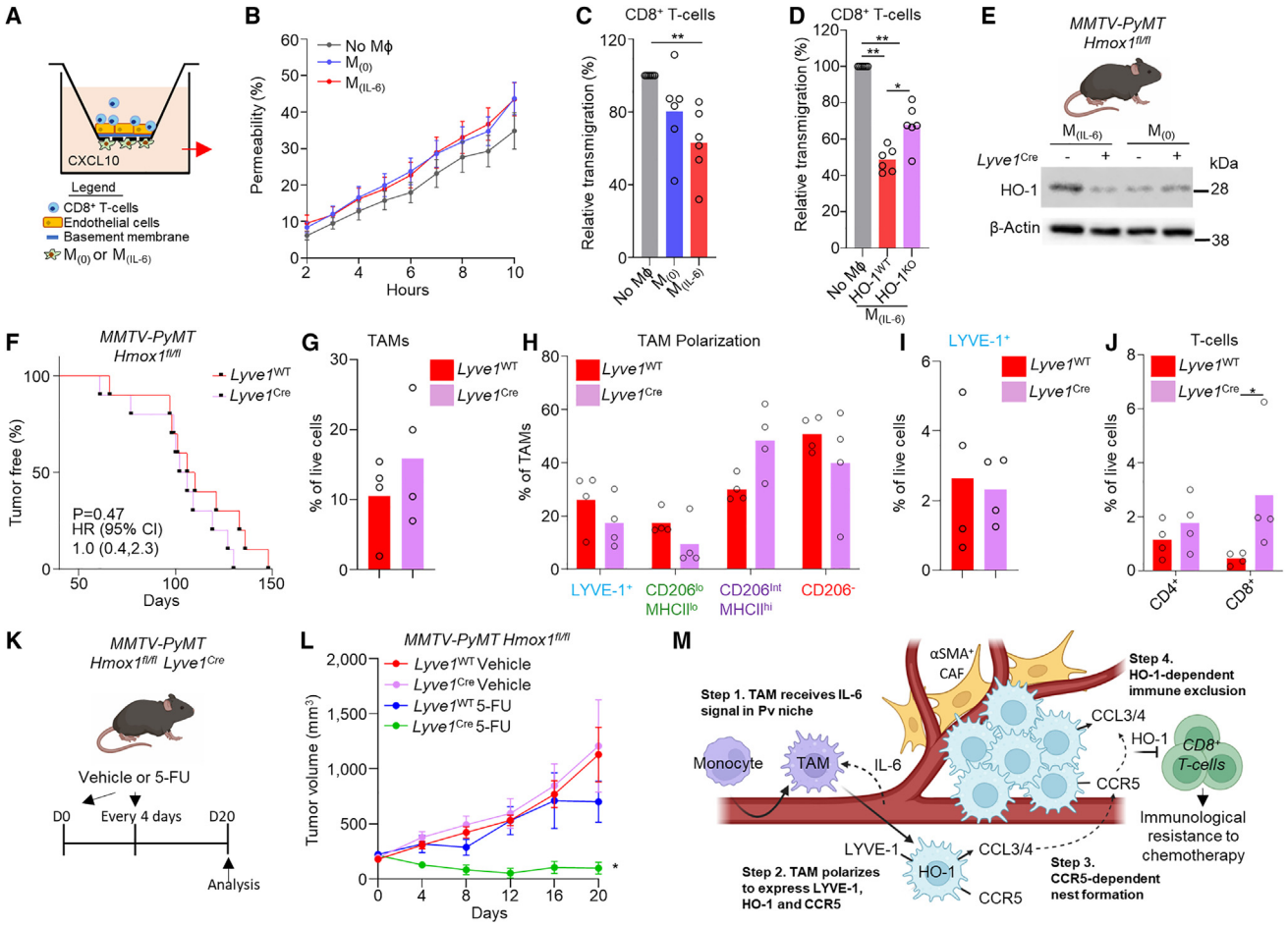

Figure 5. HO-1 expression by LYVE-1⁺ TAMs facilitates immune exclusion and resistance to chemotherapy

(A–D) An *in vitro* Pv niche assay was established to investigate the role of Pv macrophages in CD8⁺ T cell transendothelial migration. A schematic of the assay (A). Permeability of the endothelial cell layer at the indicated time points to albumin in the presence or absence of $M_{(0)}$ or $M_{(IL\text{-}6)}$ cells (B). The relative transendothelial migration of CD8⁺ T cells in the presence or absence of $M_{(0)}$ or $M_{(IL\text{-}6)}$ cells on the basolateral surface (C), and the effect of genetic knockout of HO-1 ($HO\text{-}1^{KO}$) in $M_{(IL\text{-}6)}$ (using *Hmox1*$^{fl/fl}$ x *Lyz2*^{cre} mice) (D).

(E) Western blot for HO-1 and β-actin expressions in BMDMs under $M_{(0)}$ (MCF alone) and IL-6 polarization ($M_{(IL\text{-}6)}$) conditions from *MMTV-PyMT* x *Hmox1*$^{fl/fl}$ mice with (*Lyve1*^{Cre}) or without (*Lyve1*^{WT}) Cre-recombinase driven from the *Lyve1* promoter.

(F) Kaplan-Meier curve showing the tumor latency for *Lyve1*^{WT} (n = 10) and *Lyve1*^{Cre} (n = 10) mice; HR, hazard ratio.

(G–J) Tumors from *Lyve1*^{WT} and *Lyve1*^{Cre} mice were enzyme dispersed and assessed using flow cytometry for the abundance of live (7AAD⁻) CD45⁺F4/80⁺Ly6C⁻ TAMs (G) and their phenotype as proportions of the TAM gate (H) and the abundance of LYVE-1⁺ TAMs as the percentage of live cells (I) and CD8⁺ and CD4⁺ T cells (J) (n = 4 per group).

(K and L) Schematic representing the dosing strategy for 5-FU in tumor-bearing *Lyve1*^{WT} and *Lyve1*^{Cre} mice (K). Growth curves of established spontaneous tumors that were given vehicle or 5-FU (40 mg/kg/4 days) where indicated. Indicated dosing started at day 0 (cohorts of n = 5–7 mice) (L).

(M) Schematic overview of the Pv niche and stepwise development and function of LYVE-1⁺ TAMs. Images in (E), (K), and (M) were created using *BioRender* software.

Bar charts show the mean, and the dots show individual data points from individual tumors and mice. Line charts display the mean and SEM. * $p < 0.05$ and ** $p < 0.01$.

and 5I). However, in concordance with the *in vitro* observations and a wider role of LYVE-1⁺ TAMs in immune exclusion, the genetic inactivation of HO-1 in LYVE-1⁺ TAMs in the Pv niche in mice resulted in an improved and selective infiltration of CD8⁺ T cells into the TME (Figure 5J). Furthermore, the loss of HO-1 activity in the LYVE-1⁺ TAM subset rendered the tumors sensitive to chemotherapy treatment (Figures 5K and 5L). Collectively, these *in vitro* and *in vivo* data suggest that LYVE-1⁺ TAMs serve as gatekeepers in modulating CD8⁺ T cell entry into the tumor, which dictates the sensitivity of the TME to the immune-stimulating effects of chemotherapy, and our data highlight HO-1 as a key effector molecule in this axis.

DISCUSSION

In this study, we describe a coordinated and collaborative role for LYVE-1⁺ PvTAMs in forming multi-cellular nest structures within the TME, which influence the immune-mediated

responses of cytotoxic chemotherapy. This study sheds light on the development of the LYVE-1$^+$ TAM subset in cancer. Using photolabeling approaches, we demonstrate that LYVE-1$^+$ TAMs develop from a progenitor cell recruited into the TME rather than a tissue-resident macrophage source, consistent with previous studies that have demonstrated that PvTAMs derive from a monocyte origin.[11,25,52] PvTAMs can develop through a sequential signaling program involving their upregulation of CXCR4 in response to tumor-cell-derived TGF-β, which guides their migration back to the endothelium on a gradient of CXCL12 expressed by a PvCAF population.[11] The importance of the CXCR4/CXCL12 axis in PvTAM accumulation at the vasculature has been demonstrated in several studies.[20,53] We propose that the mechanisms presented in this study provide insight on the subsequent developmental step of PvTAMs into the LYVE-1$^+$ TAM population post reaching the endothelium. This is supported by the observation that the loss of IL-6 resulted in a striking and specific loss of the LYVE-1$^+$ TAM population, leaving other TAM polarization states unchanged, suggesting that it is important for only the terminal step in polarization. The interaction of angiopoietin-2 expressed on ECs and Tie2 expressed on PvTAMs has also been demonstrated to play a role in their accumulation at the vasculature[54,55]; however, we did not find evidence of *Tie2/Tek* gene expression in LYVE-1$^+$ TAMs, suggesting that these cells may be a discrete subset.

We demonstrate that a key feature of the LYVE-1$^+$ TAM program was a high expression of the enzyme HO-1, a gene that we have previously linked to IL-6 signaling.[3] We identified *in vitro* that c-MAF signaling was required for LYVE-1, HO-1, and CD206 expressions on BMDMs in response to IL-6 in a STAT3/c-MAF-dependent pathway. This may explain the similarity of the population to tissue-resident macrophages, as these have recently been demonstrated to be dependent on c-MAF signaling.[37] Although the signal-inducing c-MAF in healthy tissues is unknown, it could explain the unexpected high expression of HO-1, which is generally considered as a stress- or inflammation-inducible enzyme.[51,56]

The identification of the immunological resistance mechanisms to cytotoxic chemotherapy responses are important, as it has become apparent that the immune-stimulating properties of these drugs may underlie a significant proportion of their anti-tumor efficacy.[57–62] This study also complements the wider association between TAMs playing a pivotal role in the resistance of the tumor to chemotherapeutic drugs[6–8,47] and facilitating relapse after the cessation of treatment.[20] Furthermore, this study provides further support for the link between IL-6 and the immune-stimulating effects of cytotoxic chemotherapies.[63] There are many studies that have described HO-1 as having pro-tumoral properties with important roles in immune suppression and cytoprotection.[34,51,64–68] Many of the effects of HO-1 have been attributed to its production of CO as a catabolite of heme degradation, which can modulate several signaling pathways, including p38 MAPK,[69] STAT1/3,[70] and NF-κB.[71,72] We previously demonstrated in the *MMTV-PyMT* model that HO-1 plays a pivotal role in the suppression of anti-tumor CD8$^+$ T cell responses elicited by chemotherapy in *MMTV-PyMT* mice.[47] This study builds on this previous observation to demonstrate the importance of CCR5 signaling in the chemotherapy sensitivity of the TME, a chemokine induced as part of the IL-6 polarization program of Pv LYVE-1$^+$ TAMs, which are the exclusive source of HO-1 in the TME. We show that in the absence of CCR5, the spatial arrangement and cluster of LYVE-1$^+$ TAMs in the PV niche are hindered. Collectively, these data highlight a potential link between the spatial arrangement of this TAM subset and the maintenance of an immunologically "cold" TME through CD8$^+$ T cell exclusion via an HO-1-dependent mechanism, which renders the TME resistant to the immune-stimulating effects of chemotherapy. This also highlights a potential biological function of TAMs that is associated with their ability to work in concert with one another to achieve this biological effect. It has been demonstrated that macrophage density can also relate to a "quorum licensing" of macrophage activation[73]; it would be interesting to understand how the nest structures might also influence or refine the effector function of LYVE-1$^+$ TAMs in the context of cancer.

It is clear that PvTAMs reside in unique niche arrangements to support their function, such as the described TMEs of metastasis (TMEM), where a PvTAM, a tumor cell expressing a slice variant of mammalian-enabled protein "Mena,"[74] and an EC are in direct contact to facilitate the transendothelial migration of tumor cells into the blood from the tumor.[18,75–78] Recently, an elegant study by Nalio Ramos et al.[15] demonstrated in human breast cancer that a folate receptor beta (FOLR2)$^+$cell adhesion molecule 1 (CADM1)$^-$ human leukocyte antigen-DR (HLA-DR)$^+$ PvTAM subset (which co-express *LYVE-1* and *MRC1*) was associated with CD8$^+$ T cell infiltration into the TME and *ex vivo* had the potential to prime CD8$^+$ T cell effector function. However, FOLR2$^+$ TAMs have also been associated with immune-suppressive microenvironments in hepatocellular carcinoma.[27] Interestingly, in *MMTV-PyMT* tumors, we identified two CD206$^+$ TAM subsets, which both express *Folr2* (Figure S5G). Taken together, this raises the possibility that LYVE-1$^+$CD206$^+$MHCII^{lo} and LYVE-1$^-$CD206$^+$MHCII^{hi} TAM subsets might play discrete, potentially opposing, roles in relation to modulating the immune landscape of the TME. As such, the heterogeneity of PvTAMs and their respective functions still requires further investigation.

In this study, we characterize the functionality associated with a multi-cellular LYVE-1$^+$ PvTAM structure and define an unappreciated collaborative action of these cells to form a multicellular niche, which are associated with the immune exclusion of CD8$^+$ T cells from the TME dependent on their expression of HO-1. We demonstrate that IL-6-driven CCR5 expression by LYVE-1$^+$ TAMs supports a dynamic and ongoing TAM>TAM communication axis, which is pivotal to the formation and maintenance of their nest structures. Interestingly, the blockade of CCR5 using maraviroc has been explored in patients with metastatic colorectal cancer (NCT01736813), where 4/6 patients showed a trend toward an increase in CD8$^+$ T cells within the TME.[79] Moreover, in this study, the authors identified a partial response (3/5 patients) and stable disease (1/5 patients) when maraviroc was combined with a chemotherapeutic agent.[79] Although tentative, it highlights intriguing key clinical parallels of our preclinical observations.

In summary (Figure 5M), we show that LYVE-1$^+$ TAMs derive from an IL-6 polarization program in the TME and demonstrate that the LYVE-1$^+$ TAM functions are not always autonomous but can be collaborative through their formation of nests within the Pv space using a CCR5-dependent communication axis.

We demonstrate that these multi-cellular nest structures are associated with immune exclusion in the TME, which is linked to the immune-mediated effects of cytotoxic chemotherapies. This study sheds light on the communication and niche arrangements of a TAM subset and their association with the outcome of chemotherapy, which could provide therapeutic opportunities for targeting their pro-tumoral functions in cancer.

Limitations of the study

This study demonstrates that LYVE-1$^+$ TAM expression of HO-1 facilitates immune exclusion in the tumor; however, the specific mechanism by which this exclusion occurs at the cellular/molecular level has not yet been deciphered, and additional experiments will be required to explore this. Additionally, although we validated that LYVE-1$^+$ TAM nests exist in human breast cancer, the experiments in this study were primarily conducted in mice and in a single, albeit spontaneous, murine model. Therefore, further experiments utilizing further mouse models and human breast cancer tissue (as well as other cancer tissues) would be needed to better define the inter-tumor and inter-species heterogeneity of the LYVE-1$^+$ TAM population. This study also used a range of knockout (KO) models; however, to further elucidate the biological implications, formation, and function of the LYVE-1$^+$ TAM nests, the implementation of models that would enable the KO of IL-6R or CCR5 selectively on the LYVE-1$^+$ TAM population would be a desirable next step.

STAR★METHODS

Detailed methods are provided in the online version of this paper and include the following:

- KEY RESOURCES TABLE
- RESOURCE AVAILABILITY
  - Lead contact
  - Material availability
  - Data and code availability
- EXPERIMENTAL MODEL AND STUDY PARTICIPANT DETAILS
  - Mice
  - Cell lines
  - Study approval
- METHOD DETAILS
  - Tumor studies
  - *In vitro* derived macrophage polarization and gene knockdown
  - T-cell isolation
  - *In vitro* macrophage transwell migration assay
  - *In vitro* macrophage focal-point migration assay
  - *In vitro* Pv nest transwell assay
  - Western blot
  - Immunofluorescence
  - Bioluminescence imaging
  - Flow cytometry
  - Quantitative real time PCR
  - Transcriptomic data and analysis
- QUANTIFICATION AND STATISTICAL ANALYSIS

SUPPLEMENTAL INFORMATION

Supplemental information can be found online at https://doi.org/10.1016/j.devcel.2023.06.006.

ACKNOWLEDGMENTS

The authors thank Dr. Yasmin Haque (KCL) and the NIHR BRC flow cytometry platform at Guy's and St Thomas' Biomedical Research Centre for cell sorting and flow cytometry assistance and Dr. James Levitt and the Nikon Imaging Centre (KCL) for the use of their facilities and assistance with confocal microscopy analyses. The authors would like to thank Drs. Paul Lavender, Tracey Mitchell, Gilbert Fruhwirth (KCL), and Professor Awen Gallimore (University of Cardiff) for useful discussion/advice/support; Miss Rosamond Nuamah (KCL) for running the microarray; and Mr. Stuart Newman (KCL) for help with the rederivation of the HO-1$^{Luc/EGFP}$ reporter mouse. The authors thank Professor George Kollias (University of Athens) for the use of the *Hmox1*$^{fl/fl}$ allele mice. The authors would like to thank Miss Jiaying Yao for the initial optimization of the focal-point macrophage migration assay. This work was funded by the following grants: Cancer Research UK grant DCRPGF\100009 (J.N.A.), European Research Council grant 335326 (J.N.A.), Cancer Research Institute/Wade F.B. Thompson CLIP grant (CRI3645) (J.N.A.), Medical Research Council grant MR/N013700/1 (J.E.A.), Medical Research Council grant MR/PO18823/1 (F.M.W.), Wellcome Trust grant 206439/Z/17/Z (F.M.W.), and Cancer Research UK grant C54019/A27535 (D.R.W.). The research was supported by the Cancer Research UK King's Health Partners Centre and Experimental Cancer Medicine Centre at King's College London and the National Institute for Health Research (NIHR) Biomedical Research Centre based at Guy's and St Thomas' NHS Foundation Trust and King's College London. The views expressed are those of the authors and not necessarily those of the NHS, the NIHR, or the Department of Health.

AUTHOR CONTRIBUTIONS

J.E.A. and J.N.A. conceived the project, designed the approach, performed the experiments, interpreted the data, and wrote the manuscript. K.T.F., J.W.O., I.D., H.P.M., M.B., T.S.C., K.L.-A., Z.L., D.C., J.C., D.S., R.B., T.M., Z.A., and G.L. designed the approach, performed the experiments, and interpreted the data. C.E.G., X.Z., F.M.W., T.N., J.M.B., S.K., D.R.W., and T.L. designed the experiments, interpreted the data, and provided key expertise.

DECLARATION OF INTERESTS

The authors declare no competing interests.

INCLUSION AND DIVERSITY

We support inclusive, diverse, and equitable conduct of research.

Received: June 23, 2022
Revised: April 5, 2023
Accepted: June 20, 2023
Published: July 12, 2023

REFERENCES

1. Mantovani, A., Marchesi, F., Malesci, A., Laghi, L., and Allavena, P. (2017). Tumour-associated macrophages as treatment targets in oncology. Nat. Rev. Clin. Oncol. *14*, 399–416. https://doi.org/10.1038/nrclinonc.2016.217.
2. DeNardo, D.G., Barreto, J.B., Andreu, P., Vasquez, L., Tawfik, D., Kolhatkar, N., and Coussens, L.M. (2009). CD4(+) T cells regulate pulmonary metastasis of mammary carcinomas by enhancing protumor properties of macrophages. Cancer Cell *16*, 91–102. https://doi.org/10.1016/j.ccr.2009.06.018.
3. Muliaditan, T., Caron, J., Okesola, M., Opzoomer, J.W., Kosti, P., Georgouli, M., Gordon, P., Lall, S., Kuzeva, D.M., Pedro, L., et al. (2018). Macrophages are exploited from an innate wound healing response to

facilitate cancer metastasis. Nat. Commun. *9*, 2951. https://doi.org/10.1038/s41467-018-05346-7.

4. Murray, P.J., Allen, J.E., Biswas, S.K., Fisher, E.A., Gilroy, D.W., Goerdt, S., Gordon, S., Hamilton, J.A., Ivashkiv, L.B., Lawrence, T., et al. (2014). Macrophage activation and polarization: nomenclature and experimental guidelines. Immunity *41*, 14–20. https://doi.org/10.1016/j.immuni.2014.06.008.
5. Noy, R., and Pollard, J.W. (2014). Tumor-associated macrophages: from mechanisms to therapy. Immunity *41*, 866. https://doi.org/10.1016/j.immuni.2014.09.021.
6. Paulus, P., Stanley, E.R., Schäfer, R., Abraham, D., and Aharinejad, S. (2006). Colony-stimulating factor-1 antibody reverses chemoresistance in human MCF-7 breast cancer xenografts. Cancer Res. *66*, 4349–4356. https://doi.org/10.1158/0008-5472.CAN-05-3523.
7. DeNardo, D.G., Brennan, D.J., Rexhepaj, E., Ruffell, B., Shiao, S.L., Madden, S.F., Gallagher, W.M., Wadhwani, N., Keil, S.D., Junaid, S.A., et al. (2011). Leukocyte complexity predicts breast cancer survival and functionally regulates response to chemotherapy. Cancer Discov. *1*, 54–67. https://doi.org/10.1158/2159-8274.CD-10-0028.
8. Ruffell, B., Chang-Strachan, D., Chan, V., Rosenbusch, A., Ho, C.M., Pryer, N., Daniel, D., Hwang, E.S., Rugo, H.S., and Coussens, L.M. (2014). Macrophage IL-10 blocks CD8+ T cell-dependent responses to chemotherapy by suppressing IL-12 expression in intratumoral dendritic cells. Cancer Cell *26*, 623–637. https://doi.org/10.1016/j.ccell.2014.09.006.
9. Franklin, R.A., Liao, W., Sarkar, A., Kim, M.V., Bivona, M.R., Liu, K., Pamer, E.G., and Li, M.O. (2014). The cellular and molecular origin of tumor-associated macrophages. Science *344*, 921–925. https://doi.org/10.1126/science.1252510.
10. Colegio, O.R., Chu, N.Q., Szabo, A.L., Chu, T., Rhebergen, A.M., Jairam, V., Cyrus, N., Brokowski, C.E., Eisenbarth, S.C., Phillips, G.M., et al. (2014). Functional polarization of tumour-associated macrophages by tumour-derived lactic acid. Nature *513*, 559–563. https://doi.org/10.1038/nature13490.
11. Arwert, E.N., Harney, A.S., Entenberg, D., Wang, Y., Sahai, E., Pollard, J.W., and Condeelis, J.S. (2018). A unidirectional transition from migratory to perivascular macrophage is required for tumor cell intravasation. Cell Rep. *23*, 1239–1248. https://doi.org/10.1016/j.celrep.2018.04.007.
12. Huang, Y.K., Wang, M., Sun, Y., Di Costanzo, N., Mitchell, C., Achuthan, A., Hamilton, J.A., Busuttil, R.A., and Boussioutas, A. (2019). Macrophage spatial heterogeneity in gastric cancer defined by multiplex immunohistochemistry. Nat. Commun. *10*, 3928. https://doi.org/10.1038/s41467-019-11788-4.
13. Carmona-Fontaine, C., Deforet, M., Akkari, L., Thompson, C.B., Joyce, J.A., and Xavier, J.B. (2017). Metabolic origins of spatial organization in the tumor microenvironment. Proc. Natl. Acad. Sci. USA *114*, 2934–2939. https://doi.org/10.1073/pnas.1700600114.
14. Opzoomer, J.W., Anstee, J.E., Dean, I., Hill, E.J., Bouybayoune, I., Caron, J., Muliaditan, T., Gordon, P., Sosnowska, D., Nuamah, R., et al. (2021). Macrophages orchestrate the expansion of a proangiogenic perivascular niche during cancer progression. Sci. Adv. *7*, eabg9518. https://doi.org/10.1126/sciadv.abg9518.
15. Nalio Ramos, R., Missolo-Koussou, Y., Gerber-Ferder, Y., Bromley, C.P., Bugatti, M., Núñez, N.G., Tosello Boari, J., Richer, W., Menger, L., Denizeau, J., et al. (2022). Tissue-resident FOLR2(+) macrophages associate with CD8(+) T cell infiltration in human breast cancer. Cell *185*, 1189–1207.e25. https://doi.org/10.1016/j.cell.2022.02.021.
16. Lapenna, A., De Palma, M., and Lewis, C.E. (2018). Perivascular macrophages in health and disease. Nat. Rev. Immunol. *18*, 689–702. https://doi.org/10.1038/s41577-018-0056-9.
17. Lewis, C.E., Harney, A.S., and Pollard, J.W. (2016). The multifaceted role of perivascular macrophages in tumors. Cancer Cell *30*, 365. https://doi.org/10.1016/j.ccell.2016.07.009.
18. Wyckoff, J.B., Wang, Y., Lin, E.Y., Li, J.F., Goswami, S., Stanley, E.R., Segall, J.E., Pollard, J.W., and Condeelis, J. (2007). Direct visualization of macrophage-assisted tumor cell intravasation in mammary tumors. Cancer Res. *67*, 2649–2656. https://doi.org/10.1158/0008-5472.CAN-06-1823.
19. Harney, A.S., Arwert, E.N., Entenberg, D., Wang, Y., Guo, P., Qian, B.Z., Oktay, M.H., Pollard, J.W., Jones, J.G., and Condeelis, J.S. (2015). Real-time imaging reveals local, transient vascular permeability, and tumor cell intravasation stimulated by TIE2hi macrophage-derived VEGFA. Cancer Discov. *5*, 932–943. https://doi.org/10.1158/2159-8290.CD-15-0012.
20. Hughes, R., Qian, B.Z., Rowan, C., Muthana, M., Keklikoglou, I., Olson, O.C., Tazzyman, S., Danson, S., Addison, C., Clemons, M., et al. (2015). Perivascular M2 macrophages stimulate tumor relapse after chemotherapy. Cancer Res. *75*, 3479–3491. https://doi.org/10.1158/0008-5472.CAN-14-3587.
21. Ensan, S., Li, A., Besla, R., Degousee, N., Cosme, J., Roufaiel, M., Shikatani, E.A., El-Maklizi, M., Williams, J.W., Robins, L., et al. (2016). Self-renewing resident arterial macrophages arise from embryonic CX3CR1(+) precursors and circulating monocytes immediately after birth. Nat. Immunol. *17*, 159–168. https://doi.org/10.1038/ni.3343.
22. Cho, C.H., Koh, Y.J., Han, J., Sung, H.K., Jong Lee, H., Morisada, T., Schwendener, R.A., Brekken, R.A., Kang, G., Oike, Y., et al. (2007). Angiogenic role of LYVE-1-positive macrophages in adipose tissue. Circ. Res. *100*, e47–e57. https://doi.org/10.1161/01.RES.0000259564.92792.93.
23. Pinto, A.R., Paolicelli, R., Salimova, E., Gospocic, J., Slonimsky, E., Bilbao-Cortes, D., Godwin, J.W., and Rosenthal, N.A. (2012). An abundant tissue macrophage population in the adult murine heart with a distinct alternatively-activated macrophage profile. PLoS One *7*, e36814. https://doi.org/10.1371/journal.pone.0036814.
24. Xu, H., Chen, M., Reid, D.M., and Forrester, J.V. (2007). LYVE-1-positive macrophages are present in normal murine eyes. Invest. Ophthalmol. Vis. Sci. *48*, 2162–2171. https://doi.org/10.1167/iovs.06-0783.
25. Chakarov, S., Lim, H.Y., Tan, L., Lim, S.Y., See, P., Lum, J., Zhang, X.M., Foo, S., Nakamizo, S., Duan, K., et al. (2019). Two distinct interstitial macrophage populations coexist across tissues in specific subtissular niches. Science *363*. https://doi.org/10.1126/science.aau0964.
26. Dollt, C., Becker, K., Michel, J., Melchers, S., Weis, C.A., Schledzewski, K., Krewer, A., Kloss, L., Gebhardt, C., Utikal, J., et al. (2017). The shedded ectodomain of Lyve-1 expressed on M2-like tumor-associated macrophages inhibits melanoma cell proliferation. Oncotarget *8*, 103682–103692. https://doi.org/10.18632/oncotarget.21771.
27. Sharma, A., Seow, J.J.W., Dutertre, C.A., Pai, R., Blériot, C., Mishra, A., Wong, R.M.M., Singh, G.S.N., Sudhagar, S., Khalilnezhad, S., et al. (2020). Onco-fetal reprogramming of endothelial cells drives immunosuppressive macrophages in hepatocellular carcinoma. Cell *183*, 377–394.e21. https://doi.org/10.1016/j.cell.2020.08.040.
28. Wu, S.Z., Al-Eryani, G., Roden, D.L., Junankar, S., Harvey, K., Andersson, A., Thennavan, A., Wang, C., Torpy, J.R., Bartonicek, N., et al. (2021). A single-cell and spatially resolved atlas of human breast cancers. Nat. Genet. *53*, 1334–1347. https://doi.org/10.1038/s41588-021-00911-1.
29. Jackson, D.G., Prevo, R., Clasper, S., and Banerji, S. (2001). LYVE-1, the lymphatic system and tumor lymphangiogenesis. Trends Immunol. *22*, 317–321. https://doi.org/10.1016/s1471-4906(01)01936-6.
30. Kosti, P., Opzoomer, J.W., Larios-Martinez, K.I., Henley-Smith, R., Scudamore, C.L., Okesola, M., Taher, M.Y.M., Davies, D.M., Muliaditan, T., Larcombe-Young, D., et al. (2021). Hypoxia-sensing CAR T cells provide safety and efficacy in treating solid tumors. Cell Rep. Med. *2*, 100227. https://doi.org/10.1016/j.xcrm.2021.100227.
31. Kim, J.H., Lee, S.R., Li, L.H., Park, H.J., Park, J.H., Lee, K.Y., Kim, M.K., Shin, B.A., and Choi, S.Y. (2011). High cleavage efficiency of a 2A peptide derived from porcine teschovirus-1 in human cell lines, zebrafish and mice. PLoS One *6*, e18556. https://doi.org/10.1371/journal.pone.0018556.
32. Spranger, S., Dai, D., Horton, B., and Gajewski, T.F. (2017). Tumor-residing Batf3 dendritic cells are required for effector T cell trafficking

and adoptive T cell therapy. Cancer Cell *31*, 711–723.e4. https://doi.org/10.1016/j.ccell.2017.04.003.

33. Luu Hoang, K.N., Anstee, J.E., and Arnold, J.N. (2021). The diverse roles of heme oxygenase-1 in tumor progression. Front. Immunol. *12*, 658315. https://doi.org/10.3389/fimmu.2021.658315.

34. Arnold, J.N., Magiera, L., Kraman, M., and Fearon, D.T. (2014). Tumoral immune suppression by macrophages expressing fibroblast activation protein-alpha and heme oxygenase-1. Cancer Immunol. Res. *2*, 121–126. https://doi.org/10.1158/2326-6066.CIR-13-0150.

35. Tomura, M., Yoshida, N., Tanaka, J., Karasawa, S., Miwa, Y., Miyawaki, A., and Kanagawa, O. (2008). Monitoring cellular movement in vivo with photoconvertible fluorescence protein "Kaede" transgenic mice. Proc. Natl. Acad. Sci. USA *105*, 10871–10876. https://doi.org/10.1073/pnas.0802278105.

36. Krämer, A., Green, J., Pollard, J., Jr., and Tugendreich, S. (2014). Causal analysis approaches in Ingenuity Pathway Analysis. Bioinformatics *30*, 523–530. https://doi.org/10.1093/bioinformatics/btt703.

37. Moura Silva, H., Kitoko, J.Z., Queiroz, C.P., Kroehling, L., Matheis, F., Yang, K.L., Reis, B.S., Ren-Fielding, C., Littman, D.R., Bozza, M.T., et al. (2021). c-MAF-dependent perivascular macrophages regulate diet-induced metabolic syndrome. Sci. Immunol. *6*, eabg7506. https://doi.org/10.1126/sciimmunol.abg7506.

38. Johnson, D.E., O'Keefe, R.A., and Grandis, J.R. (2018). Targeting the IL-6/JAK/STAT3 signalling axis in cancer. Nat. Rev. Clin. Oncol. *15*, 234–248. https://doi.org/10.1038/nrclinonc.2018.8.

39. Sahoo, A., Alekseev, A., Tanaka, K., Obertas, L., Lerman, B., Haymaker, C., Clise-Dwyer, K., McMurray, J.S., and Nurieva, R. (2015). Batf is important for IL-4 expression in T follicular helper cells. Nat. Commun. *6*, 7997. https://doi.org/10.1038/ncomms8997.

40. Mills, C.D., Kincaid, K., Alt, J.M., Heilman, M.J., and Hill, A.M. (2000). M-1/M-2 macrophages and the Th1/Th2 paradigm. J. Immunol. *164*, 6166–6173. https://doi.org/10.4049/jimmunol.164.12.6166.

41. Fätkenheuer, G., Pozniak, A.L., Johnson, M.A., Plettenberg, A., Staszewski, S., Hoepelman, A.I., Saag, M.S., Goebel, F.D., Rockstroh, J.K., Dezube, B.J., et al. (2005). Efficacy of short-term monotherapy with maraviroc, a new CCR5 antagonist, in patients infected with HIV-1. Nat. Med. *11*, 1170–1172. https://doi.org/10.1038/nm1319.

42. Vestweber, D. (2015). How leukocytes cross the vascular endothelium. Nat. Rev. Immunol. *15*, 692–704. https://doi.org/10.1038/nri3908.

43. Tumeh, P.C., Harview, C.L., Yearley, J.H., Shintaku, I.P., Taylor, E.J., Robert, L., Chmielowski, B., Spasic, M., Henry, G., Ciobanu, V., et al. (2014). PD-1 blockade induces responses by inhibiting adaptive immune resistance. Nature *515*, 568–571. https://doi.org/10.1038/nature13954.

44. Hamid, O., Schmidt, H., Nissan, A., Ridolfi, L., Aamdal, S., Hansson, J., Guida, M., Hyams, D.M., Gómez, H., Bastholt, L., et al. (2011). A prospective phase II trial exploring the association between tumor microenvironment biomarkers and clinical activity of ipilimumab in advanced melanoma. J. Transl. Med. *9*, 204. https://doi.org/10.1186/1479-5876-9-204.

45. Hong, M., Puaux, A.L., Huang, C., Loumagne, L., Tow, C., Mackay, C., Kato, M., Prévost-Blondel, A., Avril, M.F., Nardin, A., et al. (2011). Chemotherapy induces intratumoral expression of chemokines in cutaneous melanoma, favoring T-cell infiltration and tumor control. Cancer Res. *71*, 6997–7009. https://doi.org/10.1158/0008-5472.CAN-11-1466.

46. Ladoire, S., Mignot, G., Dabakuyo, S., Arnould, L., Apetoh, L., Rébé, C., Coudert, B., Martin, F., Bizollon, M.H., Vanoli, A., et al. (2011). In situ immune response after neoadjuvant chemotherapy for breast cancer predicts survival. J. Pathol. *224*, 389–400. https://doi.org/10.1002/path.2866.

47. Muliaditan, T., Opzoomer, J.W., Caron, J., Okesola, M., Kosti, P., Lall, S., Van Hemelrijck, M., Dazzi, F., Tutt, A., Grigoriadis, A., et al. (2018). Repurposing tin mesoporphyrin as an immune checkpoint inhibitor shows therapeutic efficacy in preclinical models of cancer. Clin. Cancer Res. *24*, 1617–1628. https://doi.org/10.1158/1078-0432.CCR-17-2587.

48. Longley, D.B., Harkin, D.P., and Johnston, P.G. (2003). 5-fluorouracil: mechanisms of action and clinical strategies. Nat. Rev. Cancer *3*, 330–338. https://doi.org/10.1038/nrc1074.

49. Ugel, S., Peranzoni, E., Desantis, G., Chioda, M., Walter, S., Weinschenk, T., Ochando, J.C., Cabrelle, A., Mandruzzato, S., and Bronte, V. (2012). Immune tolerance to tumor antigens occurs in a specialized environment of the spleen. Cell Rep. *2*, 628–639. https://doi.org/10.1016/j.celrep.2012.08.006.

50. Cao, Z., Zhang, Z., Huang, Z., Wang, R., Yang, A., Liao, L., and Du, J. (2014). Antitumor and immunomodulatory effects of low-dose 5-FU on hepatoma 22 tumor-bearing mice. Oncol. Lett. *7*, 1260–1264. https://doi.org/10.3892/ol.2014.1856.

51. Gozzelino, R., Jeney, V., and Soares, M.P. (2010). Mechanisms of cell protection by heme oxygenase-1. Annu. Rev. Pharmacol. Toxicol. *50*, 323–354. https://doi.org/10.1146/annurev.pharmtox.010909.105600.

52. De Palma, M., Venneri, M.A., Galli, R., Sergi Sergi, L., Politi, L.S., Sampaolesi, M., and Naldini, L. (2005). Tie2 identifies a hematopoietic lineage of proangiogenic monocytes required for tumor vessel formation and a mesenchymal population of pericyte progenitors. Cancer Cell *8*, 211–226. https://doi.org/10.1016/j.ccr.2005.08.002.

53. Welford, A.F., Biziato, D., Coffelt, S.B., Nucera, S., Fisher, M., Pucci, F., Di Serio, C., Naldini, L., De Palma, M., Tozer, G.M., et al. (2011). TIE2-expressing macrophages limit the therapeutic efficacy of the vascular-disrupting agent combretastatin A4 phosphate in mice. J. Clin. Invest. *121*, 1969–1973. https://doi.org/10.1172/JCI44562.

54. Harney, A.S., Karagiannis, G.S., Pignatelli, J., Smith, B.D., Kadioglu, E., Wise, S.C., Hood, M.M., Kaufman, M.D., Leary, C.B., Lu, W.P., et al. (2017). The selective Tie2 inhibitor rebastinib blocks recruitment and function of Tie2(Hi) macrophages in breast cancer and pancreatic neuroendocrine tumors. Mol. Cancer Ther. *16*, 2486–2501. https://doi.org/10.1158/1535-7163.MCT-17-0241.

55. Mazzieri, R., Pucci, F., Moi, D., Zonari, E., Ranghetti, A., Berti, A., Politi, L.S., Gentner, B., Brown, J.L., Naldini, L., et al. (2011). Targeting the ANG2/TIE2 axis inhibits tumor growth and metastasis by impairing angiogenesis and disabling rebounds of proangiogenic myeloid cells. Cancer Cell *19*, 512–526. https://doi.org/10.1016/j.ccr.2011.02.005.

56. Ryter, S.W., and Choi, A.M. (2009). Heme oxygenase-1/carbon monoxide: from metabolism to molecular therapy. Am. J. Respir. Cell Mol. Biol. *41*, 251–260. https://doi.org/10.1165/rcmb.2009-0170TR.

57. Casares, N., Pequignot, M.O., Tesniere, A., Ghiringhelli, F., Roux, S., Chaput, N., Schmitt, E., Hamai, A., Hervas-Stubbs, S., Obeid, M., et al. (2005). Caspase-dependent immunogenicity of doxorubicin-induced tumor cell death. J. Exp. Med. *202*, 1691–1701. https://doi.org/10.1084/jem.20050915.

58. Geary, S.M., Lemke, C.D., Lubaroff, D.M., and Salem, A.K. (2013). The combination of a low-dose chemotherapeutic agent, 5-fluorouracil, and an adenoviral tumor vaccine has a synergistic benefit on survival in a tumor model system. PLoS One *8*, e67904. https://doi.org/10.1371/journal.pone.0067904.

59. Bracci, L., Schiavoni, G., Sistigu, A., and Belardelli, F. (2014). Immune-based mechanisms of cytotoxic chemotherapy: implications for the design of novel and rationale-based combined treatments against cancer. Cell Death Differ. *21*, 15–25. https://doi.org/10.1038/cdd.2013.67.

60. Pfirschke, C., Engblom, C., Rickelt, S., Cortez-Retamozo, V., Garris, C., Pucci, F., Yamazaki, T., Poirier-Colame, V., Newton, A., Redouane, Y., et al. (2016). Immunogenic chemotherapy sensitizes tumors to checkpoint blockade therapy. Immunity *44*, 343–354. https://doi.org/10.1016/j.immuni.2015.11.024.

61. Opzoomer, J.W., Sosnowska, D., Anstee, J.E., Spicer, J.F., and Arnold, J.N. (2019). Cytotoxic chemotherapy as an immune stimulus: A molecular perspective on turning up the immunological heat on cancer. Front. Immunol. *10*, 1654. https://doi.org/10.3389/fimmu.2019.01654.

62. Sistigu, A., Yamazaki, T., Vacchelli, E., Chaba, K., Enot, D.P., Adam, J., Vitale, I., Goubar, A., Baracco, E.E., Remédios, C., et al. (2014). Cancer cell-autonomous contribution of type I interferon signaling to the efficacy

of chemotherapy. Nat. Med. *20*, 1301–1309. https://doi.org/10.1038/nm.3708.

63. Bent, E.H., Millán-Barea, L.R., Zhuang, I., Goulet, D.R., Fröse, J., and Hemann, M.T. (2021). Microenvironmental IL-6 inhibits anti-cancer immune responses generated by cytotoxic chemotherapy. Nat. Commun. *12*, 6218. https://doi.org/10.1038/s41467-021-26407-4.
64. Tan, Q., Wang, H., Hu, Y., Hu, M., Li, X., Aodengqimuge, M., Ma, Y., Wei, C., and Song, L. (2015). Src/STAT3-dependent heme oxygenase-1 induction mediates chemoresistance of breast cancer cells to doxorubicin by promoting autophagy. Cancer Sci. *106*, 1023–1032. https://doi.org/10.1111/cas.12712.
65. Nuhn, P., Künzli, B.M., Hennig, R., Mitkus, T., Ramanauskas, T., Nobiling, R., Meuer, S.C., Friess, H., and Berberat, P.O. (2009). Heme oxygenase-1 and its metabolites affect pancreatic tumor growth in vivo. Mol. Cancer *8*, 37. https://doi.org/10.1186/1476-4598-8-37.
66. Nowis, D., Bugajski, M., Winiarska, M., Bil, J., Szokalska, A., Salwa, P., Issat, T., Was, H., Jozkowicz, A., Dulak, J., et al. (2008). Zinc protoporphyrin IX, a heme oxygenase-1 inhibitor, demonstrates potent antitumor effects but is unable to potentiate antitumor effects of chemotherapeutics in mice. BMC Cancer *8*, 197. https://doi.org/10.1186/1471-2407-8-197.
67. Di Biase, S., Lee, C., Brandhorst, S., Manes, B., Buono, R., Cheng, C.W., Cacciottolo, M., Martin-Montalvo, A., de Cabo, R., Wei, M., et al. (2016). Fasting-mimicking diet reduces HO-1 to promote T cell-mediated tumor cytotoxicity. Cancer Cell *30*, 136–146. https://doi.org/10.1016/j.ccell.2016.06.005.
68. Berberat, P.O., Dambrauskas, Z., Gulbinas, A., Giese, T., Giese, N., Künzli, B., Autschbach, F., Meuer, S., Büchler, M.W., and Friess, H. (2005). Inhibition of heme oxygenase-1 increases responsiveness of pancreatic cancer cells to anticancer treatment. Clin. Cancer Res. *11*, 3790–3798. https://doi.org/10.1158/1078-0432.CCR-04-2159.
69. Otterbein, L.E., Bach, F.H., Alam, J., Soares, M., Tao Lu, H., Wysk, M., Davis, R.J., Flavell, R.A., and Choi, A.M. (2000). Carbon monoxide has anti-inflammatory effects involving the mitogen-activated protein kinase pathway. Nat. Med. *6*, 422–428. https://doi.org/10.1038/74680.
70. Zhang, X., Shan, P., Alam, J., Fu, X.Y., and Lee, P.J. (2005). Carbon monoxide differentially modulates STAT1 and STAT3 and inhibits apoptosis via a phosphatidylinositol 3-kinase/Akt and p38 kinase-dependent STAT3 pathway during anoxia-reoxygenation injury. J. Biol. Chem. *280*, 8714–8721. https://doi.org/10.1074/jbc.M408092200.
71. Cepinskas, G., Katada, K., Bihari, A., and Potter, R.F. (2008). Carbon monoxide liberated from carbon monoxide-releasing molecule CORM-2 attenuates inflammation in the liver of septic mice. Am. J. Physiol. Gastrointest. Liver Physiol. *294*, G184–G191. https://doi.org/10.1152/ajpgi.00348.2007.
72. Megías, J., Busserolles, J., and Alcaraz, M.J. (2007). The carbon monoxide-releasing molecule CORM-2 inhibits the inflammatory response induced by cytokines in Caco-2 cells. Br. J. Pharmacol. *150*, 977–986. https://doi.org/10.1038/sj.bjp.0707184.
73. Muldoon, J.J., Chuang, Y., Bagheri, N., and Leonard, J.N. (2020). Macrophages employ quorum licensing to regulate collective activation. Nat. Commun. *11*, 878. https://doi.org/10.1038/s41467-020-14547-y.
74. Goswami, S., Philippar, U., Sun, D., Patsialou, A., Avraham, J., Wang, W., Di Modugno, F., Nistico, P., Gertler, F.B., and Condeelis, J.S. (2009). Identification of invasion specific splice variants of the cytoskeletal protein Mena present in mammary tumor cells during invasion in vivo. Clin. Exp. Metastasis *26*, 153–159. https://doi.org/10.1007/s10585-008-9225-8.
75. Roh-Johnson, M., Bravo-Cordero, J.J., Patsialou, A., Sharma, V.P., Guo, P., Liu, H., Hodgson, L., and Condeelis, J. (2014). Macrophage contact induces RhoA GTPase signaling to trigger tumor cell intravasation. Oncogene *33*, 4203–4212. https://doi.org/10.1038/onc.2013.377.
76. Robinson, B.D., Sica, G.L., Liu, Y.F., Rohan, T.E., Gertler, F.B., Condeelis, J.S., and Jones, J.G. (2009). Tumor microenvironment of metastasis in human breast carcinoma: a potential prognostic marker linked to hematogenous dissemination. Clin. Cancer Res. *15*, 2433–2441. https://doi.org/10.1158/1078-0432.CCR-08-2179.
77. Rohan, T.E., Xue, X., Lin, H.M., D'Alfonso, T.M., Ginter, P.S., Oktay, M.H., Robinson, B.D., Ginsberg, M., Gertler, F.B., Glass, A.G., et al. (2014). Tumor microenvironment of metastasis and risk of distant metastasis of breast cancer. J. Natl. Cancer Inst. *106*. https://doi.org/10.1093/jnci/dju136.
78. Sparano, J.A., Gray, R., Oktay, M.H., Entenberg, D., Rohan, T., Xue, X., Donovan, M., Peterson, M., Shuber, A., Hamilton, D.A., et al. (2017). A metastasis biomarker (MetaSite Breast™ Score) is associated with distant recurrence in hormone receptor-positive, HER2-negative early-stage breast cancer. NPJ Breast Cancer *3*, 42. https://doi.org/10.1038/s41523-017-0043-5.
79. Halama, N., Zoernig, I., Berthel, A., Kahlert, C., Klupp, F., Suarez-Carmona, M., Suetterlin, T., Brand, K., Krauss, J., Lasitschka, F., et al. (2016). Tumoral immune cell exploitation in colorectal cancer metastases can be targeted effectively by anti-CCR5 therapy in cancer patients. Cancer Cell *29*, 587–601. https://doi.org/10.1016/j.ccell.2016.03.005.
80. Stuart, T., Butler, A., Hoffman, P., Hafemeister, C., Papalexi, E., Mauck, W.M., 3rd, Hao, Y., Stoeckius, M., Smibert, P., and Satija, R. (2019). Comprehensive integration of single-cell data. Cell *177*, 1888–1902.e21. https://doi.org/10.1016/j.cell.2019.05.031.
81. Pliner, H.A., Shendure, J., and Trapnell, C. (2019). Supervised classification enables rapid annotation of cell atlases. Nat. Methods *16*, 983–986. https://doi.org/10.1038/s41592-019-0535-3.
82. Elso, C.M., Roberts, L.J., Smyth, G.K., Thomson, R.J., Baldwin, T.M., Foote, S.J., and Handman, E. (2004). Leishmaniasis host response loci (lmr1-3) modify disease severity through a Th1/Th2-independent pathway. Genes Immun. *5*, 93–100. https://doi.org/10.1038/sj.gene.6364042.
83. Guy, C.T., Cardiff, R.D., and Muller, W.J. (1992). Induction of mammary tumors by expression of polyomavirus middle T oncogene: a transgenic mouse model for metastatic disease. Mol. Cell. Biol. *12*, 954–961.
84. Tzima, S., Victoratos, P., Kranidioti, K., Alexiou, M., and Kollias, G. (2009). Myeloid heme oxygenase-1 regulates innate immunity and autoimmunity by modulating IFN-beta production. J. Exp. Med. *206*, 1167–1179. https://doi.org/10.1084/jem.20081582.
85. Skarnes, W.C., Rosen, B., West, A.P., Koutsourakis, M., Bushell, W., Iyer, V., Mujica, A.O., Thomas, M., Harrow, J., Cox, T., et al. (2011). A conditional knockout resource for the genome-wide study of mouse gene function. Nature *474*, 337–342. https://doi.org/10.1038/nature10163.
86. Dutton, E.E., Gajdasik, D.W., Willis, C., Fiancette, R., Bishop, E.L., Camelo, A., Sleeman, M.A., Coccia, M., Didierlaurent, A.M., Tomura, M., et al. (2019). Peripheral lymph nodes contain migratory and resident innate lymphoid cell populations. Sci. Immunol. *4*. https://doi.org/10.1126/sciimmunol.aau8082.
87. Kraman, M., Bambrough, P.J., Arnold, J.N., Roberts, E.W., Magiera, L., Jones, J.O., Gopinathan, A., Tuveson, D.A., and Fearon, D.T. (2010). Suppression of antitumor immunity by stromal cells expressing fibroblast activation protein-alpha. Science *330*, 827–830. https://doi.org/10.1126/science.1195300.
88. Qian, B.Z., Li, J., Zhang, H., Kitamura, T., Zhang, J., Campion, L.R., Kaiser, E.A., Snyder, L.A., and Pollard, J.W. (2011). CCL2 recruits inflammatory monocytes to facilitate breast-tumour metastasis. Nature *475*, 222–225. https://doi.org/10.1038/nature10138.
89. Bolstad, B.M., Irizarry, R.A., Astrand, M., and Speed, T.P. (2003). A comparison of normalization methods for high density oligonucleotide array data based on variance and bias. Bioinformatics *19*, 185–193.

STAR★METHODS

KEY RESOURCES TABLE

REAGENT or RESOURCE	SOURCE	IDENTIFIER
Antibodies		
Rabbit anti-β-actin	Abcam	Cat# ab8227; RRID: AB_2305186
Rabbit anti-HO-1	Proteintech	Cat# 10701-1-AP; RRID: AB_2118685
Rabbit anti-c-MAF	Abcam	Cat# ab77071; RRID: AB_1951643
Rabbit anti-STAT3 (clone 79D7)	Cell Signaling Technology	Cat# 4904; RRID: AB_331269
Goat anti-rabbit immunoglobulins/HRP	Agilent Dako	Cat# P0448; RRID: AB_2617138
Rabbit anti-αSMA	AnaSpec	Cat# AS-29553; RRID: AB_2120181
Rabbit anti-CD31	Abcam	Cat# ab28364; RRID: AB_726362
Rat anti-mouse CD31 (clone ER-MP12)	Thermo Fisher Scientific	Cat# MA1-40074; RRID: AB_1072120
Rabbit anti-human CD31 (clone EP3095)	Abcam	Cat# ab134168; RRID: AB_2890012
Mouse anti-CD68 (clone KP1)	Invitrogen	Cat# MA5-13324; RRID: AB_10987212
Rat anti-mouse F4/80 (clone Cl:A3-1)	Bio-RAD	Cat# MCA497; RRID: AB_323806
Goat anti-HO-1	R&D systems	Cat# AF3776; RRID: AB_2295362
Rabbit anti-LYVE-1	Abcam	Cat# ab33682; RRID: AB_881387
Donkey anti-rabbit IgG (H+L) Alexa Fluor® 488	Thermo Fisher Scientific	Cat# A32790; RRID: AB_2762833
Donkey anti-rat IgG (H+L) Alexa Fluor® 488	Thermo Fisher Scientific	Cat# A-21208; RRID: AB_2535794
Donkey anti-goat IgG (H+L) Alexa Fluor® 488	Thermo Fisher Scientific	Cat# A-11055; RRID: AB_2534102
Donkey anti-rabbit IgG (H+L) Alexa Fluor® 568	Thermo Fisher Scientific	Cat# A10042; RRID: AB_2534017
Donkey anti-goat IgG (H+L) Alexa Fluor® 568	Thermo Fisher Scientific	Cat# A-11057; RRID: AB_2534104
Donkey anti-rabbit IgG (H+L) Alexa Fluor® 647	Thermo Fisher Scientific	Cat# A-31573; RRID: AB_2536183
Donkey anti-mouse IgG (H+L) Alexa Fluor® 647	Thermo Fisher Scientific	Cat# A-31571; RRID: AB_162542
Goat anti-rat IgG NorthernLights™ NL637	R&D systems	Cat# NL014; RRID: AB_884218
Donkey anti-sheep IgG (H+L) Cy™ 3	Jackson ImmunoResearch	Cat# 713-165-147; RRID: AB_2315778
Armenian hamster anti-mouse CCR5 PE (clone HM-CCR5 (7A4))	Thermo Fisher Scientific	Cat# 12-1951-82; RRID: AB_657684
Armenian hamster anti-mouse CD3ε APC (clone 145-2C11)	Thermo Fisher Scientific	Cat# MA1-10186; RRID: AB_11153519
Armenian hamster anti-mouse CD3ε PE (clone 145-2C11)	Thermo Fisher Scientific	Cat# A14714; RRID: AB_2534230
Rat anti-mouse CD3ε Brilliant Violet 421™ (clone 17A2)	Biolegend®	Cat# 100227; RRID: AB_10900227
Rat anti-mouse CD3ε PE/Cyanine 7 (clone 145-2C11)	Biolegend®	Cat# 100319; RRID: AB_312684
Rat anti-mouse CD4 APC (clone RM4-5)	Thermo Fisher Scientific	Cat# 17-0042-82; RRID: AB_469323
Rat anti-mouse CD4 FITC (clone RM4-5)	Thermo Fisher Scientific	Cat# 11-0042-82; RRID: AB_464896
Rat anti-mouse CD4 PE (clone RM4-5)	BD Biosciences	Cat# 553048; RRID: AB_394584
Rat anti-mouse CD8α Brilliant Violet 421™ (clone 53-5.7)	Biolegend®	Cat# 100737; RRID: AB_10897101
Rat anti-mouse CD8a Brilliant Violet 711 ™ (clone 53-5.7)	Biolegend®	Cat# 100759; RRID: AB_2563510
Rat anti-mouse CD8α FITC (clone 53-5.7)	Biolegend®	Cat# 100705; RRID: AB_312744
Rat anti-mouse CD8β FITC (clone H35-17.2)	Thermo Fisher Scientific	Cat# 11-0083-82 RRID: AB_657764
Rat anti-mouse CD8β eFluor ™ 450 (clone H35-17.2)	Thermo Fisher Scientific	Cat# 48-0083-82 RRID: AB_11218504
Rat anti-mouse CD11b Brilliant Violet 510 ™ (clone M1/70)	Biolegend®	Cat# 101245; RRID: AB_2561390
Armenian hamster anti-mouse CD11c APC (clone N418)	Thermo Fisher Scientific	Cat# 17-0114-82; RRID: AB_469346

(*Continued on next page*)

Continued

REAGENT or RESOURCE	SOURCE	IDENTIFIER
Armenian hamster anti-mouse CD11c FITC (clone N418)	Biolegend®	Cat# 117305; RRID: AB_313774
Purified anti-mouse CD16 / CD32 (Fc Shield) (clone 2.4G2)	Tonbo Biosciences	Cat# 70-0161; RRID: AB_2621487
Rat anti-mouse CD19 Brilliant Violet 421 ™ (clone 6D5)	Biolegend®	Cat# 115537; RRID: AB_10895761
Rat anti-mouse CD19 APC (clone 6D5)	Biolegend®	Cat# 115511; RRID: AB_313646
Rat anti-mouse CD19 FITC (clone 1D3/CD19)	Biolegend®	Cat# 152403; RRID: AB_2629812
Rat anti-mouse CD31 FITC (clone 390)	Thermo Fisher Scientific	Cat# RM5201; RRID: AB_10373983
Rat anti-mouse CD31 PE (clone 390)	Thermo Fisher Scientific	Cat# 12-0311-82; RRID: AB_465632
Rat anti-mouse CD31 BD Horizon ™ BV510 (clone MEC 13.3)	BD biosciences	Cat# 563089; RRID: AB_2737997
Rat anti-mouse CD45 APC (clone 30-F11)	Thermo Fisher Scientific	Cat# 17-0451-82; RRID: AB_469392
Rat anti-mouse CD45 APC-eFluor® 780 (clone 30-F11)	Thermo Fisher Scientific	Cat# 47-0451-82; RRID: AB_1548781
Rat anti-mouse CD45 Brilliant Violet 605 ™ (clone 30-F11)	Biolegend®	Cat# 103139; RRID: AB_2562341
Rat anti-mouse CD45 Brilliant Violet 510 ™ (clone 30-F11)	Biolegend®	Cat# 103137; RRID: AB_2561392
Mouse anti-mouse CD90.1 (Thy-1.1) eFluor ™ 450 (clone HIS51)	Thermo Fisher Scientific	Cat# 48-0900-82; RRID: AB_1272254
Mouse anti-mouse CD90.1 (Thy-1.1) Brilliant Violet 510™ (clone OX-7)	Biolegend®	Cat# 202535; RRID: AB_2562643
Rat anti-mouse CD90.2 (Thy-1.2) eFluor ™ 450 (clone 53-2.1)	Thermo Fisher Scientific	Cat# 48-0902-82; RRID: AB_1272200
Rat anti-mouse CD90.2 (Thy-1.2) Brilliant Violet 510™ (clone 53-2.1)	Biolegend®	Cat# 140319; RRID: AB_2561395
Rat anti-mouse CD206 APC (clone C068C2)	Biolegend®	Cat# 141707; RRID: AB_10896057
Rat anti-mouse CD206 FITC (clone C068C2)	Biolegend®	Cat# 141703; RRID: AB_10900988
Rat anti-mouse CD206 Brilliant Violet 785™ (clone C068C2)	Biolegend®	Cat# 141729; RRID: AB_2565823
Goat anti-mouse CD206 APC	Bio-Techne	Cat# FAB2535A; RRID: AB_10971650
Rat anti-mouse F4/80 APC (clone BM8)	Thermo Fisher Scientific	Cat# 17-4801-82; RRID: AB_2784648
Rat anti-mouse F4/80 APC-eFluor® 780 (clone BM8)	Thermo Fisher Scientific	Cat# 47-4801-82; RRID: AB_2735036
Rat anti-mouse F4/80 PE (clone BM8)	Thermo Fisher Scientific	Cat# 12-4801-82; RRID: AB_465923
Rat anti-mouse F4/80 eFluor ™ 660 (clone BM8)	Thermo Fisher Scientific	Cat# 50-4801-82; RRID: AB_11149361
Rat anti-mouse F4/80 Brilliant Violet 421 ™ (clone BM8)	Biolegend®	Cat# 123132; RRID: AB_11203717
Rat anti-mouse F4/80 Brilliant Violet 510 ™ (clone BM8)	Biolegend®	Cat# 123135; RRID: AB_2562622
Rat anti-mouse F4/80 FITC (clone BM8)	Biolegend®	Cat# 123107; RRID: AB_893500
Rat anti-mouse Gr-1 FITC (clone RB6-8C5)	Biolegend®	Cat# 108405; RRID: AB_313370
Mouse anti-human Granzyme-B PE (clone GB11)	Thermo Fisher Scientific	Cat# GRB04; RRID: AB_1500188
Rat anti-mouse ICAM-1 Brilliant Violet 421™ (clone YN1/1.7.4)	Biolegend®	Cat# 116141; RRID: AB_2876428
Rat anti-mouse IFN-γ APC (clone XMG1.2)	Thermo Fisher Scientific	Cat# 17-7311-82; RRID: AB_469504
Rat anti-mouse Ki-67 Alexa Flour® 700 (clone SolA15)	Thermo Fisher Scientific	Cat# 56-5698-00 RRID: AB_2637480
Rat anti-mouse Ly6C APC (clone HK1.4)	Thermo Fisher Scientific	Cat# 17-5932-82; RRID: AB_1724153
Rat anti-mouse Ly6C APC-eFluor® 780 (clone HK1.4)	Thermo Fisher Scientific	Cat# 47-5932-82; RRID: AB_2573992
Rat anti-mouse Ly6C eFluor ™ 450 (clone HK1.4)	Thermo Fisher Scientific	Cat# 48-5932-82; RRID: AB_10805519
Rat anti-mouse Ly6C PE (clone HK1.4)	Thermo Fisher Scientific	Cat# 12-5932-82; RRID: AB_10804510
Rat anti-mouse Ly6C FITC (clone HK1.4)	Biolegend®	Cat# 128005; RRID: AB_1186134
Rat anti-mouse Ly6G APC (clone 1A8)	Biolegend®	Cat# 127613; RRID: AB_1877163
Rat anti-mouse LYVE-1 Alexa Fluor® 488 (clone ALY7)	Thermo Fisher Scientific	Cat# 53-0443-82; RRID: AB_1633415
Rat anti-mouse LYVE-1 PE (clone ALY7)	Thermo Fisher Scientific	Cat# 12-0443-82; RRID: AB_2802179

(*Continued on next page*)

Continued

REAGENT or RESOURCE	SOURCE	IDENTIFIER
Rat anti-mouse LYVE-1 APC (clone 223322)	Bio-Techne	Cat# FAB2125A; RRID: AB_10972770
Rat anti-mouse MHCII PE (clone M5/114.15.2)	Thermo Fisher Scientific	Cat# 12-5321-82; RRID: AB_465928
Rat anti-mouse MHCII Brilliant Violet 421 ™ (clone M5/114.15.2)	Biolegend®	Cat# 107631; RRID: AB_10900075
Rat anti-mouse MHCII Brilliant Violet 510 ™ (clone M5/114.15.2)	Biolegend®	Cat# 107635; RRID: AB_2561397
Rat anti-mouse MHCII FITC (clone M5/114.15.2)	Biolegend®	Cat# 107605; RRID: AB_313320
Mouse anti-mouse NK1.1 APC (clone PK136)	Thermo Fisher Scientific	Cat# 17-5941-82; RRID: AB_469479
Rat anti-mouse PNAd Alexa Fluor® 647 (clone MECA-79)	Biolegend®	Cat# 120807; RRID: AB_2783059
Rat anti-mouse TNFα PE (clone MP6-XT22)	Thermo Fisher Scientific	Cat# 12-7321-82; RRID: AB_466199
Rat anti-mouse VCAM-1 PE (clone 429 (MVCAM.A))	Biolegend®	Cat# 105713; RRID: AB_1134166
Rat anti-mouse TER-119 PerCP-Cy5.5 (clone TER-119)	Thermo Fisher Scientific	Cat# 45-5921-82; RRID: AB_925765
Rat anti-mouse CD8α (clone 53-6.7)	Biolegend®	Cat# 100768; RRID: AB_2616823
Armenian hamster anti-mouse CD3ε (clone 145-2C11)	Thermo Fisher Scientific	Cat# 16-0031-82; RRID: AB_468847
Syrian hamster anti-mouse CD28 (Clone 37.51)	Thermo Fisher Scientific	Cat# 16-0281-82; RRID: AB_468921
Bacterial and virus strains		
E. coli (DH10B competent cells)	Thermo Fisher Scientific	Cat# EC0113
Biological samples		
Human breast adenocarcinoma tissue	King's Health Partners Cancer Biobank	REC reference 12/EE/0493
Chemicals, peptides, and recombinant proteins		
Proteinase K	Sigma-Aldrich	Cat# SAE0151
FCS	Thermo Fisher Scientific	Cat# 26170043
Spectinomycin	Sigma-Aldrich	Cat# S0692
LR Clonase™ II Plus enzyme mix	Thermo Fisher Scientific	Cat# 12538120
Trypan blue	Sigma-Aldrich	Cat# T8154
Maraviroc	Cayman	Cat# 14641
5-Fluorouracil	Sigma-Aldrich	Cat# F6627
Collagenase I from Clostridium Histolyticum	Sigma-Aldrich	Cat# C0130
BSA	Sigma-Aldrich	Cat# BSAV-RO
EDTA	Sigma-Aldrich	Cat# E8008
Penicillin/streptomycin	Sigma-Aldrich	Cat# P4333
Deoxyribonuclease I	AppliChem	Cat# A3778
RBC lysis buffer	Roche	Cat# 11814389001
Recombinant murine M-CSF	Bio-Techne	Cat# 416-ML
Recombinant murine IL-4	Bio-Techne	Cat# 404-ML
Recombinant murine IL-6	Bio-Techne	Cat# 406-ML
Recombinant murine IFN-γ	Bio-Techne	Cat# 485-MI
Recombinant murine CCL4	Bio-Techne	Cat# 451-MB
LPS from *E.coli*	Sigma-Aldrich	Cat# L2630
Lipofectamine™ RNAiMAX	Thermo Fisher Scientific	Cat# 13778075
2-mercaptoethanol	Sigma-Aldrich	Cat# M6250
Recombinant murine IL-2	Bio-Techne	Cat# 402-ML
Basement Membrane Extract	Cultrex	Cat# 3432-010-01
Recombinant murine CXCL10	Bio-Techne	Cat# 466-CR
SeeBlue™ Plus2 pre-stained makers	Thermo Fisher Scientific	Cat# LC5925
Tween 20	Sigma-Aldrich	Cat# P1379
Luminata™ Crescendo Western HRP substrate	Millipore	Cat# WBLUR
Donkey serum	Sigma-Aldrich	Cat# D9663
Triton X-100	Sigma-Aldrich	Cat# X100
FITC-conjugated dextran (2,000,000 MW)	Thermo Fisher Scientific	Cat# D7137

(*Continued on next page*)

Continued

REAGENT or RESOURCE	SOURCE	IDENTIFIER
4',6-diamidino-2-phenylindole,dihydrochloride (DAPI)	Thermo Fisher Scientific	Cat# D1306
7-amino actinomycin D (7AAD)	Sigma-Aldrich	Cat# A9400
Fixable Viability Dye eFluor® 780	Thermo Fisher Scientific	Cat# 65-0865-14
Near-IR Dead cell staining kit	Thermo Fisher Scientific	Cat# L34976
Mm-IL6 probe	Bio-Techne	Cat# 315898
XenoLight D-luciferin	PerkinElmer	Cat# 122799
Critical commercial assays		
Sequal PrepTM Long PCR kit	Thermo Fisher Scientific	Cat# A10498
MycoAlert Mycoplasma Detection Kit	Lonza	Cat# LT07-218
Anti-PE MicroBeads	Miltenyi Biotec	Cat# 130-048-801
MidiMacs separator	Miltenyi Biotec	Cat# 130-042-302
LS columns	Miltenyi Biotec	Cat# 130-042-401
CD8a+ T-cell isolation Kit, mouse	Miltenyi Biotec	Cat# 130-104-075
AccuCheck counting beads	Thermo Fisher Scientific	Cat# PCB100
Pierce™ BCA Protein Assay Kit	Thermo Fisher Scientific	Cat# 23225
RNAscope Multiplex Fluorescent Reagent Kit v2 Assay	Bio-Techne	Cat# 323100-USM
Opal™ 570 Reagent Pack	Akoya Biosciences	Cat# FP1488001KT
PureLink® RNA Mini Kit	Invitrogen	Cat# 12183020
Ovation® PicoSL WTA system V2	Tecan	Cat# 3312
Encore® BiotinIL Module	Tecan	Cat# 4200
Whole-Genome Gene Expression Direct Hybridisation Assay	Illumina	Cat# BD-901-1002
CellTracker™ Deep Red Dye	Thermo Fisher Scientific	Cat# C34565
Foxp3 Transcription Factor Staining Buffer Set	Thermo Fisher Scientific	Cat# 00-5523-00
Deposited data		
Microarray dataset	This paper	GEO: GSE192911
Bulk RNA-seq dataset	Opzoomer et al.[14]	GEO: GSE160561
scRNA-seq dataset	Opzoomer et al.[14]	GEO: GSE160641
Microarray dataset	Muliaditan et al.[3]	GEO: GSE113034
Experimental models: Cell lines		
3B-11 murine endothelial cells	ATCC	Cat# CRL-2160; RRID: CVCL_5487
4T1 mammary adenocarcinoma cells	ATCC	Cat# CRL-2539; RRID: CVCL_0125
Experimental models: Organisms/strains		
MMTV-PyMT (FVB/N background)	The Jackson Laboratory	RRID: IMSR_JAX:002374
WT Balb/c	Charles River	RRID: IMSR_CRL:028
WT C57BL/6	Charles River	RRID: IMSR_CRL:027
homozygous $Il6^{-/-}$ (B6.129S2-Il6tm1Kopf/J) C57BL/6	The Jackson Laboratory	RRID: IMSR_JAX:002650
$Ccr5^{-/-}$ (B6.129P2-Ccr5tm1Kuz/J) C57BL/6	The Jackson Laboratory	RRID: IMSR_JAX:005427
Lyz2-cre (B6.129P2-Lyz2tm1(cre)^{Ifo}/J) C57BL/6	The Jackson Laboratory	RRID: IMSR_JAX:004781
C57Bl/6 homozygous *Kaede*	Professor Michio Tomura, Osaka Ohtani University, Osaka, Japan	N/A
Hmox1$^{fl/fl}$	Professor George Kollias, Biomedical Sciences Research Center "Alexander Fleming", Athens, Greece	N/A
HO-1$^{Luc/EGFP}$	This paper	N/A
Oligonucleotides		
ON-TARGETplus SMARTpool siRNA targeting *c-Maf*	Horizon Discovery Ltd	Cat# J-040681-10-0005
ON-TARGETplus SMARTpool siRNA targeting *Stat3*	Horizon Discovery Ltd	Cat# J-040794-10-0005

(*Continued on next page*)

Continued

REAGENT or RESOURCE	SOURCE	IDENTIFIER
ON-TARGETplus SMARTpool siRNA targeting *Hmox1*	Horizon Discovery Ltd	Cat# J-040543-12
ON-TARGETplus non-targeting siRNA	Horizon Discovery Ltd	Cat# (D-001810-01-05
Il6 gene expression assay	Thermo Fisher Scientific	Cat# 4331182; Assay ID Mm00446190_m1
Tbp gene expression assay	Thermo Fisher Scientific	Cat# 4331182; Assay ID Mm01277045_m1
Recombinant DNA		
Flp mRNA	Miltenyi Biotech	Cat# 130-106-769
Software and algorithms		
NIS Elements Advanced Research software	Nikon	https://www.microscope.healthcare.nikon.com/products/software/nis-elements/nis-elements-advanced-research
Cell counter	ImageJ-plugin	https://imagej.nih.gov/ij/plugins/cell-counter.html
Analyze Spheroid Cell Invasion In 3D Matrix	ImageJ-macro	https://github.com/MontpellierRessourcesImagerie/imagej_macros_and_scripts/wiki/Analyze-Spheroid-Cell-Invasion-In-3D-Matrix
FlowJo v.10 Software	Tree Star, Inc; BD biosciences	https://www.flowjo.com/
Living Image Software	PerkinElmer	https://www.perkinelmer.com/product/spectrum-200-living-image-v4series-1-128113
QIAGEN IPA software	QIAGEN Inc; Krämer et al.[36]	https://digitalinsights.qiagen.com/IPA
R version 4.0.2	The R Project for Statistical Computing	https://www.r-project.org/
Seurat v3 R package	Stuart et al.[80]	https://satijalab.org/seurat/
Garnett package	Pliner et al.[81]	
GraphPad Prism 8 software	GraphPad	https://www.graphpad.com/scientific-software/prism/
Partek® Genomics Suite® software	Partek	https://www.partek.com/partek-genomics-suite/
"CompareGrowthCurves" function of the statmod software package	Elso et al.[82]	https://rdrr.io/cran/statmod/man/growthcurve.html

RESOURCE AVAILABILITY

Lead contact

Further information and requests for resources and reagents should be directed to and will be fulfilled by the Lead Contact Dr James Arnold (james.arnold@kcl.ac.uk).

Material availability

Mice and reagents generated in this study will be made available from the Lead Contact for academic/non-commercial research purposes on request under a Material Transfer Agreement.

Data and code availability

The RNA-seq transcriptomic and microarray datasets that support the findings of this study are available through the Gene Expression Omnibus; GSE160561, GSE160641, GSE113034. The microarray datasets are available at GSE192911. The authors declare that all other data supporting the findings of this study are available within the paper and its supplementary information files. Any additional information required to reanalyze the data reported in this paper is available from the Lead Contact upon request.

EXPERIMENTAL MODEL AND STUDY PARTICIPANT DETAILS

Mice

Mice used in this study were housed under specific pathogen-free conditions in individually ventilated cages at a temperature of 21°C with water and food *ad libitum*. Wild type mice used in this study were female and 4-6 weeks-old on either a Balb/c or C57BL/6 background and obtained from Charles River. Transgenic mice used in the study included homozygous Il6$^{-/-}$ (B6.129S2-Il6tm1-Kopf/J), Ccr5$^{-/-}$ (B6.129P2-Ccr5tm1Kuz/J), *Lyz2*-Cre (B6.129P2-Lyz2tm1(cre)^{Ifo}/J) and *Lyve-1-cre* (B6;129P2-*Lyve1tm1.1(EGFP/cre)Cys* /J) were on a C57BL/6 background and *MMTV-PyMT* mice were on FVB/N background[83] and obtained from The Jackson Laboratory. Where indicated, female KO mice were crossed with male *MMTV-PyMT* mice and the F2 homozygous or F2 WT offspring used experimentally. Female C57Bl/6 homozygous *Kaede* mice[35] were crossed with male *MMTV-PyMT* (FVB background) mice and the F1 offspring were used experimentally. Cohort sizes were informed by prior studies.[3,47] The *Hmox1*$^{fl/fl}$ and *Lyz2* (Lysozyme M) or *Lyve-1* driven Cre-recombinase were crossed for the *MMTV-PyMT/Hmox1*$^{fl/fl}$*Lyz2*^{Cre}[84] or *MMTV-PyMT/Hmox1*$^{fl/fl}$*Lyve1*^{Cre} (referred to as *Lyve1*^{Cre} mice in the manuscript). *Hmox1*$^{fl/fl}$ mice were a gift from Professor George Kollias, Biomedical Sciences Research Center "Alexander Fleming", Athens, Greece. All mice used for experiments were female and randomly assigned to treatment groups. Mice were approximately 21-26 g when tumors became palpable. Experiments were performed in at least duplicate and for spontaneous *MMTV-PyMT* tumor studies individual mice were collected on separate days and all data points are presented. End points for tumor studies were assessed on a welfare assessment, however, were typically when the primary tumor reached 1500mm^3 (unless stated otherwise). For generation of HO-1-Luciferace-EGFP- knock-in mouse (HO-1$^{Luc/EGFP}$) we have used BAC (Bacterial Artificial Chromosomes) recombineering strategy.[85] A synthetic cassette containing P2A-Luciferase-P2A-EGFP-Stop-FRT-βAct-Neo-pA-FRT sequence was inserted before the endogenous stop codon of *Hmox1* in BACs that correspond to *Hmox1* locus. The insert-containing BAC was further subcloned into pR3R4ccdB plasmid that contains gateway sites. The resulting ''intermediate'' vector contains ~5kb 5' and 3' homology arms and was used for generation of the final vector by modular vector assembly by the gateway method. The gateway reaction was performed using LR Clonase™ II Plus enzyme mix (Thermo Fisher Scientific) according to the manufacturers' protocol. The intermediate targeting vector was combined with pL3/L4 (DTA selection cassette) and incubated at 25°C overnight (O.N.). After treatment with Proteinase K (Sigma-Aldrich), the reaction mix was transformed into chemically competent *E. coli* (DH10B, Thermo Fisher Scientific) and plated onto YEG (yeast extract with glucose) agar plates containing 4-chlorophenylalanine and spectinomycin antibiotic (Sigma-Aldrich) (25 μg/mL). Individual colonies were picked and verified with restriction digestion quality control and sequenced across all recombineered junctions. A positive final targeting vector was linearized at *AsiSI* restriction site and electroporated to C57BL/6J embryonic stem (ES) cells. Clones were selected and picked under G418 antibiotic selection. Genomic DNA from positively selected ES cell clones were further screened with long range and short-range PCR for target recombination, 5' and 3' homology arms using the Sequal Prep™ Long PCR kit (Thermo Fisher Scientific). The neomycin selection cassette, which was flanked by flippase (Flp) recombination target sites, was removed by fertilizing WT C57BL/6 oocytes with sperm from HO-1$^{Luc/EGFP}$ mice. Six hours after insemination, fertilized zygotes were identified by the presence of pronuclei (87%) and received a cytoplasmic injection of Flp mRNA (Miltenyi Biotech). Injected zygotes were surgically transferred to CD-1 0.5dpc pseudopregnant recipient females. Long range PCR confirmed successful recombination.

Cell lines

3B-11 murine endothelial cells and 4T1 mammary adenocarcinoma were obtained from ATCC. Cell lines were confirmed to be mycoplasma free using the MycoAlert Mycoplasma Detection Kit (Lonza) and were cultured in RPMI (Gibco) supplemented with 10% FCS (Thermo Fisher Scientific).

Study approval

All experiments involving animals were approved by the Animal and Welfare and Ethical Review Board of King's College London or the University of Birmingham and the Home Office UK. Human breast adenocarcinoma tissue was obtained with informed consent under ethical approval from the King's Health Partners Cancer Biobank (REC reference 12/EE/0493).

METHOD DETAILS

Tumor studies

4T1 (Balb/c) cells were orthotopically implanted for tumors (to generate splenic tumor-derived, but TME naive, monocytes for *in vitro* studies). A total of 2.5 x 10^5 cells in 100 μL RPMI were injected subcutaneously into the mammary fat pad of syngeneic female mice. In *MMTV-PyMT* mice, tumors arose spontaneously. When tumors became palpable, volumes were measured every 2-4 days using digital caliper measurements of the long (L) and short (S) dimensions of the tumor. Tumor volume was established using the following equation: Volume= (S^2xL)/2. *MMTV-PyMT Kaede* mice were photolabeled under anesthesia. Individual tumors were exposed to a violet light (405nm wavelength) through the skin for a total of nine 20 second exposure cycles with a short 5 second break interval between each cycle. Black cardboard was used to shield the rest of the mouse throughout the photoconversion procedure. Mice for 0 h time points were culled immediately after photoconversion. This photoconversion approach was adapted from that used to label peripheral lymph nodes[86] and was optimized for *MMTV-PyMT* tumors.[14] Tumor tissue for flow cytometry analyses was enzyme-digested to release single cells as previously described.[47,87] In brief, tissues were minced using scalpels, and then single

cells were liberated by incubation for 60 mins at 37°C with 1 mg/mL Collagenase I from *Clostridium Histolyticum* (Sigma-Aldrich) and 0.1 mg/mL Deoxyribonuclease I (AppliChem) in RPMI. Released cells were then passed through a 70 μm cell strainer prior to staining for flow cytometry analyses. Viable cells were numerated using a hemocytometer with trypan blue (Sigma-Aldrich) exclusion. For drug treatments, drugs were freshly prepared on the day of injection and administered by intraperitoneal (i.p.) injection using a 26 G needle. Maraviroc (Cayman) was solubilized in ethanol and diluted with saline and administered to mice i.p. using a bi-daily dose of 10mg/kg. 5-Fluorouracil (Sigma-Aldrich) was prepared fresh and dissolved in saline at 6 mg/mL and injected to mice i.p. at 40 mg/kg/4 days. Immune-depleted mice were injected i.p. every 4 days, starting 48 h prior to the commencement of treatment, with 400 μg of anti-CD8α (53-6.7) (Biolegend®).

In vitro derived macrophage polarization and gene knockdown

Murine bone marrow (BM) was flushed from the femur and tibia of non tumor bearing WT C57Bl/6 mice using a syringe and needle. Splenocytes for monocyte isolation were acquired from spleens of 4T1 tumor bearing mice by crushing through a 70 μm pore strainer. RBC were lysed using RBC lysis buffer (Roche). Ly6C$^+$ monocytes were isolated from the splenocytes by blocking Fc receptors using 5 μg/mL anti-CD16/32 (2.4G2, Tonbo Biosciences) prior to staining with Ly6C PE (HK1.4; Thermo Fisher Scientific) in MACs buffer (DPBS (Thermo Fisher Scientific), 0.5% BSA (Sigma-Aldrich), 2mM EDTA (Sigma-Aldrich)) at 1 μg/mL, followed by anti-PE MicroBeads (Miltenyi Biotec) and isolated using a MidiMacs separator and LS columns (Miltenyi Biotec) according to the manufacturers' protocol. BM cells or isolated Ly6C$^+$ monocytes were plated in RPMI, 10% FCS, 1 x penicillin/streptomycin (Sigma-Aldrich), 10 ng/mL recombinant murine M-CSF (Bio-Techne) at 1 x 10^6 cells/well on 6 well plates for 72 h prior to subsequent downstream mRNA and protein analyses. Where viable macrophages were required for ongoing experiments, 5.5 x 10^6 BM cells were plated at day 0 on 6 cm non tissue culture-treated plates in the above macrophage culture media. Additional murine cytokines, IL-4, IL-6, IFN-γ (Bio-Techne) and/or LPS from *Escherichia Coli* (Sigma-Aldrich) were added where indicated in the figure legends at 50 ng/mL unless stated otherwise. After 72 h in culture, macrophage purity was assessed by flow cytometry. Macrophages differentiated in the presence of M-CSF alone were referred to as $M_{(0)}$ cells, and macrophages differentiated in the presence of M-CSF and IL-6 were labelled $M_{(IL\text{-}6)}$ cells. For siRNA knock down experiments, $M_{(0)}$ macrophages had their media changed to IMDM, 10% FCS and 10 ng/mL M-CSF. In an Eppendorf, ON-TARGET$_{plus}$ SMARTpool siRNA (Horizon Discovery Ltd) targeting *c-Maf* (J-040681-10-0005) *Stat3* (J-040794-10-0005), *Hmox1* (J-040543-12) or ON-TARGET$_{plus}$ non-targeting siRNA (D-001810-01-05), were added to 250 μL of Opti-MEM (Thermo Fisher Scientific) at a concentration of 100 pmol. To each respective tube, an equal volume of Opti-MEM mixed with 5 μL Lipofectamine^{TM} RNA$_{iMAX}$ (Thermo Fisher Scientific) was added and incubated for 20 mins at room temperature (RT). The transfection mixture was then drop-wise added to $M_{(0)}$ BMDMs. The wells were gently mixed until the siRNA transfection buffer distributed evenly and incubated for 96 h to allow for protein knock down in the presence or absence of polarizing cytokines at 25 ng/mL as indicated.

T-cell isolation

For isolating murine T-cells, spleens were excised from WT C57Bl/6 mice and placed in RPMI, 10% FCS, 20 μM 2-mercaptoethanol (Sigma-Aldrich), 1X penicillin/streptomycin. Spleens were crushed through a 70 μm pore strainer and washed through using RPMI. Liberated splenocytes were centrifuged at 500 x *g* for 3 mins and the cell pellet was re-suspended in 1 mL of red blood cell lysis buffer (Roche) for 2 mins at RT. Cells were then re-centrifuged at 500 x *g* for 3 mins and the pellet was resuspended in RPMI. Live cells were numerated using Trypan blue exclusion on a hemocytometer. CD8$^+$ T-cells were purified using the CD8a$^+$ T-cell isolation Kit, mouse (Miltenyi Biotec) and isolated using a MidiMacs separator and LS columns (Miltenyi Biotec) according to the manufacturers' protocol. T-cells were resuspended in T-cell culture media that was further supplemented with 2 ng/mL recombinant murine IL-2 (Bio-Techne) and purified CD8$^+$ T-cells were plated at a density of 0.1x10^6 cells/well in 200 μL onto a high binding 96-well plate (Sigma-Aldrich) that had been pre-coated O.N. with a mix of anti-mouse CD3ε (145-2C11, 5 μg/mL) and anti-mouse CD28 (37.51, 3 μg/mL) antibodies in sterile DPBS (100 μL/well) at 4ºC. After 48 h CD8$^+$ T-cells were transferred to a fresh uncoated plate and rested for at least 48 h before being numerated and used for down-stream *in vitro* assays.

In vitro macrophage transwell migration assay

$M_{(0)}$ and $M_{(IL\text{-}6)}$ BMDMs were prepared as described above from WT or Ccr5$^{-/-}$ C57BL/6 mice. Macrophages were removed from the plate using 1 mL of enzyme-free dissociation media (Thermo Fisher Scientific). $M_{(0)}$ or $M_{(IL\text{-}6)}$ cells were fluorescently labelled using CellTracker^{Tm} deep red dye (Thermo Fisher Scientific) and suspended at 1x10^6/mL in RPMI, 10% FCS (complete media) and 100 μL was transferred onto a 8 μm pore transwell insert (Corning) sitting in 24-well plate. After 10-minute incubation at 37°C, 5% CO_2, 600 μL of complete media with/without 50 ng/mL recombinant murine CCL4 (Bio-Techne) was added to the well. After 24-hour incubation at 37°C, 5% CO_2, the transwell insert was removed and the medium in the well was transferred to a FACS tube. The wells were washed with PBS 0.5% (w/v) BSA to ensure all the cells were collected. Collected cells were centrifuged and the cell pellet was resuspended in 200 μL PBS 0.5% (w/v) BSA. 20 μL of AccuCheck counting beads (Thermo Fisher Scientific) was added to each tube prior to FACS analysis. Counts of labelled viable cells and beads were determined using FlowJo software. Migrated cells concentration (cell/μL) was then calculated based on the manufacturers' manual. Relative migration was normalized using the CCL4 sample against the paired control.

In vitro macrophage focal-point migration assay

$M_{(0)}$ macrophages were generated as described above and removed from the plate using 1 mL of enzyme-free dissociation media (Thermo Fisher Scientific) and mechanically detaching the cells using a cell scrapper. The resultant solutions were centrifuged at 2000 x *g* for 3 mins and resuspended at a concentration of 10,000 cells/mL in 80% RPMI (inc.10%FCS) and 20% methylcellulose with 10 ng/mL M-CSF. To prepare a methylcellulose stock solution; autoclaved methylcellulose (Sigma-Aldrich) was dissolved at 24 g/L in pre-heated serum-free RPMI media for 2 mins at 60°C. After this, the solution was diluted with 2 volumes of RT serum-free RPMI and then mixed O.N. at 4°C. The final solution was cleared by centrifugation at 5000 x *g* for 2 h at RT. To the lid of an inverted petri dish, 25 μL drops of macrophages were placed, the lid was carefully inverted and placed on top of a DPBS filled petri dish. The dish was incubated for 24 h to allow the formation of macrophage spheroids within the hanging drop. Subsequently, media containing spheroids were collected in Eppendorf tubes using DPBS. The spheroids were allowed to briefly settle in the bottom of the Eppendorf tubes after which the DPBS was carefully removed and the spheroids were placed in wells containing RPMI, 10% FCS, 10 ng/mL M-CSF with or without 25 ng/mL IL-6 and placed in a 37ºC 5% CO_2 incubator to allow attachment and eventual spreading. Images of spheroid cultures was performed using the live cell Eclipse Ti-2 inverted microscope in the Nikon Imaging Centre at King's College London. NIS Elements Advanced Research software (Nikon) was used to process the images. Total area of spheroids was measured using the "Analyze Spheroid Cell Invasion In 3D Matrix" macro in ImageJ, and cell number was counted using the "Cell counter" plugin in ImageJ.

In vitro Pv nest transwell assay

Transwell assays were conducted with transwell inserts with 8 μm pores (Corning) for migration studies and 0.4 μm pores (Corning) for permeability studies. Inserts were coated with Basement Membrane Extract (Cultrex) diluted 1:100 in RPMI for 1 h at RT. Excess Basement Membrane Extract was aspirated and 2 x 10^4 3B-11 endothelial cells were seeded onto the apical side of the transwell insert in RPMI supplemented with 10% FCS and left to attach for 24 h. Media was removed, the whole plate inverted and 10^5 $M_{(0)}$ or $M_{(IL\text{-}6)}$ BMDMs were seeded onto the basolateral side of the transwell membrane in RPMI supplemented with 10% FCS and left to attach for 2 h at 37°C. Subsequently, the plate was reinverted to its original position and RPMI supplemented with 10% FCS, 10 ng/mL M-CSF with or without 10 ng/mL IL-6 added to the apical and basolateral space. After cells were left to interact for 24 h at 37°C, 4 x 10^5 $CD8^+$ T cells (which had been prior incubated on anti-CD3 and -CD28 coated plated to develop effector function) were added to the inserts in RPMI, 10% FCS and 100 ng/mL with murine CXCL10 (Bio-Techne) spiked into the wells. After 16 h, migrated cells were collected from the well and stained for flow cytometry analysis and quantification with AccuCheck counting beads (Thermo Fisher Scientific). The permeability assay was performed as described previously.[88] In brief, permeability of the *in vitro* Pv niche was measured using 4% (w/v) Evans Blue-conjugated Bovine Serum Albumin (BSA) diluted in DPBS was placed into the apical transwell chamber while phenol red-free RPMI, 10% FCS was added to the basolateral chamber. Presence of Evans Blue-BSA in the basolateral chamber was assessed at indicated time-points by absorbance at 620 nm on a NanoDrop™ spectrophotometer (Thermo Fisher Scientific). These experiments were performed in the presence or absence of 10 ng/mL IL-6 and M-CSF.

Western blot

Cells were lysed and SDS PAGE/western blots were conducted as previously described.[3] In brief, cells were lysed in the well using western blot lysis buffer 0.1M Tris-hydrochloride pH 6.8, with 20% glycerol and 4% sodium dodecyl sulphate containing 1X protease and phosphatase inhibitor cocktail (Thermo Fisher Scientific). All tubes were heated at 95°C for 15 mins to break down DNA. Protein concentration was then determined using the Pierce™ BCA Protein Assay Kit (Thermo Fisher Scientific) using the manufacturers' protocol. Samples were then run under reducing conditions on 12% bis-tris sodium dodecyl sulphate polyacrylamide gel electrophoresis (SDS-PAGE) gels alongside SeeBlue™ Plus2 pre-stained makers (Thermo Fisher Scientific). SDS-PAGE gels were then transferred onto polyvinyl-difluoride (PVDF) membranes which were subsequently blocked in 100 mM Tris, 140 mM NaCl, 0.1% Tween 20 (Sigma-Aldrich), pH7.4 (TBS-T) containing 5% skimmed milk at RT for 1 h. Primary antibodies were applied at 4°C O.N. and secondary antibodies for 1 h at RT. Wash steps to remove unbound antibodies were 3 x 20 mins in TBS-T. The following primary antibodies were used: rabbit anti-β-actin, 1:5,000 (ab8227, Abcam), rabbit anti-HO-1 1:1,000 (10701-1-AP, Proteintech), rabbit anti-c-MAF 1:1,000 (ab77071, Abcam), rabbit anti-STAT3 1:2000 (clone 79D7, Cell Signaling Technology). These antibodies were detected using goat anti-rabbit immunoglobulins/HRP secondary antibody 1:2,000 (Agilent Dako). Protein bands were detected using Luminata™ Crescendo Western HRP substrate (Millipore) and CL-XPosure™ Film (Thermo Fisher Scientific).

Immunofluorescence

Mouse mammary tumor tissue or human in invasive ductal carcinoma tissue was fixed O.N. in 4% paraformaldehyde, followed by O.N. dehydration in 30% sucrose prior to embedding in OCT and snap freezing absolute ethanol and dry ice. Sections from the embedded tumors (10 μm) were placed onto microscope slides were incubated further in 4% paraformaldehyde in DPBS for 10 mins at RT prior to washing in TBS-T and blocked using TBS-T, 10% donkey serum (Sigma-Aldrich), 0.2% Triton X-100 (Sigma-Aldrich). Immunofluorescence staining was performed as previously described.[3] Antibodies against the following targets and their dilutions were used as follows; αSMA 1:100 (AS-29553, AnaSpec), CD31 1:100 (ab28364 Abcam), CD31 1:100 (MA1-40074, Thermo Fisher Scientific), CD31 1:100 (EP3095, Abcam), CD68 1:100 (KP1, Invitrogen), F4/80 1:100 (C1:A3-1, Bio-Rad), HO-1 1:100 (AF3776, R&D systems), HO-1 1:100 (10701-1-AP, Proteintech), LYVE-1 1:100 (ab33682, Abcam). Primary antibodies were detected using antigen specific donkey IgG, used at 1:200: AlexaFluor® 488 anti-rabbit IgG, AlexaFluor® 488 anti-rat IgG,

AlexaFluor® 488 anti-goat IgG, AlexaFluor® 568 anti-rabbit IgG, AlexaFluor® 568 anti-goat IgG, AlexaFluor® 647 anti-rabbit IgG (Thermo Fisher Scientific), AlexaFluor® 647 anti-mouse IgG, NL637 anti-rat goat IgG (R&D Systems) and Cy3® anti-sheep IgG (Jackson ImmunoResearch). Viable blood vessels were visualized in mice through intravenous (i.v.) injection of FITC-conjugated dextran (2,000,000 MW, Thermo Fisher Scientific) 20 mins prior to sacrifice. Nuclei were stained using 1.25 μg/mL 4',6-diamidino-2-phenylindole,dihydrochloride (DAPI) (Thermo Fisher Scientific). RNA scope was performed on formalin-fixed paraffin-embedded (FFPE) *MMTV-PyMT* tumor sections as per manufacturers' instructions using the RNAscope® Multiplex Fluorescent Reagent Kit v2 Assay (Bio-Techne; 323100-USM). The Mm-IL6 (Bio-Techne; 315898) probe was used and was detected using the Opal™ 570 Reagent Pack (FP1488001KT, Akoya Biosciences). Following RNAscope, immunofluorescence imaging was performed as previously described above. Images were acquired using a Nikon Eclipse Ti-E Inverted spinning disk confocal. For 5-color confocal microscopy, images were acquired on a Nikon A1R spectral deconvolution confocal microscope. Using a 32-channel A1-GasAsP-detector unit, fluorochrome emission can be split up in up to 32 bands from 400 to 750 nm with a spectral discrimination of 10 or 20 nm bandwidth when excited by a laser-box with 4 solid state lasers 405, 488, 561 and 640 nm. The acquisition signals were then clearly and reliably distinguished by a process called ''spectral unmixing''. Images were analyzed using the NIS-Elements software.

Bioluminescence imaging

For assessing Luc bio-distribution *in vivo* mice were injected i.p. with 3 mg XenoLight D-luciferin (PerkinElmer) in sterile DPBS 10 mins prior to imaging. For whole-body imaging animals were anesthetized and placed in the *in vivo* Imaging System (IVIS®) Lumina Series III (PerkinElmer). For imaging the Luc bio-distribution of different tissues, the mice were injected with D-luciferin and sacrificed after 10 mins and the dissected tissues were then imaged 15 mins later. To quantify luminescence, a region of interest (ROI) was drawn around a specific area and total photon flux (PF) (photon/second; p/s) was measured. All data was analyzed using the Living Image Software (PerkinElmer).

Flow cytometry

Flow cytometry was performed as previously described.[34] The following antibodies against the indicated antigen were purchased from Thermo Fisher Scientific and were used at 1 μg/mL unless stated otherwise: CCR5 PE (HM-CCR5(7A4)), CD3ε APC, PE, PE-Cy7 (145-2C11) and Brilliant Violet (BV)421 (17A2; Biolegend®), CD4 APC, FITC and PE (RM4-5), CD8α BV421, BV711 and FITC (53-6.7; Biolegend®), CD8β FITC and eFluor®450 (H35-17.2), CD11b BV510 (M1/70; Biolegend®), CD11c APC (N418) and FITC (N418; Biolegend®), CD16/32 (2.4G2; Tonbo Biosciences), CD19 BV421, APC (6D5; Biolegend®) and FITC (1D3/CD19; Biolegend®), CD31 FITC, PE (390) and BV510 (MEC 13.3; BD biosciences), CD45 BV605 (30-F11; Biolegend®), APC, APC-eFluor® 780 (30-F11), BV510 and BV785 (30-F11; Biolegend®), CD90.1 eFluor® 450 (HIS51) and BV510 (OX-7; Biolegend®), CD90.2 eFluor® 450 and BV510 (53-2.1; Biolegend®), CD206 APC, FITC and BV785 (C068C2; Biolegend®) and APC (FAB2535A; Bio-Techne), F4/80 APC, APC-eFluor® 780, PE and eFluor® 660, BV421 and FITC (BM8; Biolegend®), Gr-1 FITC (RB6-8C5; Biolegend®), Granzyme-B PE (GB11), ICAM-1 BV421 (YN1/1.7.4, Biolegend®), IFN-γ APC (XMG1.2), Ki-67 AF700 (SolA15), Ly6C APC, APC-eFluor® 780, eFluor®450 and FITC (HK1.4; Biolegend®), Ly6G APC (1A8; Biolegend®), LYVE-1 Alexa Fluor® 488, PE (ALY7) and APC (FAB2125A; Bio-Techne), MHCII PE, BV421, BV510 and FITC (M5/114.15.2; Biolegend®), NK1.1 APC (PK136), PNAd AF647 (MECA-79, Biolegend®), TNF-α PE (MP6-XT22), VCAM-1 PE (429 (MVCAM.A), Biolegend®). Positive stains were compared to fluorescence minus one (FMO) controls. Intracellular stains were performed as previously described[34] using the Foxp3 Transcription factor staining buffer set (Thermo Fisher Scientific). Dead cells and red blood cells were excluded using 1 μg/mL 7-amino actinomycin D (7AAD; Sigma-Aldrich), Fixable Viability Dye eFluor® 780 or Near-IR Dead cell staining kit (Thermo Fisher Scientific) or DAPI alongside anti-Ter-119 PerCP-Cy5.5 (Ter-119). Data were collected on a BD FACS Canto II (BD Biosciences). Cells were sorted on a BD FACSAria (BD biosciences). Data was analyzed using FlowJo software (BD biosciences). Immune cells ($CD45^+$) were separated based upon the following surface characteristics: $CD11c^+F4/80^-$ (dendritic cells), $CD11b^+F4/80^{hi}$ (macrophages), $F4/80^{-/lo}Ly6G^-Ly6C^+$ (monocytes), $CD11b^+Ly6G^+$ (neutrophils), $NK1.1^+$ (NK/NKT-cells), $CD3\varepsilon^+$ (T cells), $CD3\varepsilon^+CD4^+$ ($CD4^+$ T cells), $CD3\varepsilon^+$(or FSC-A^{low})$CD8\alpha/\beta^+$ ($CD8^+$ T cells), $CD3\varepsilon^-CD19^+$ (B cells). Cancer associated fibroblasts (CAFs) were identified as $CD45^-$ $Thy1^+$ cells and tumor cells were identified as $CD45^-Thy1^-CD31^-$.

Quantitative real time PCR

mRNA was extracted and quantitative reverse transcription PCR was performed as previously described[34] using the following primers/probes purchased from (Thermo Fisher Scientific): *Il6* Mm00446190_m1 and *Tbp* Mm01277045_m1. Expression is represented relative to the house-keeping gene Tata-binding protein (*Tbp*). Gene expression was measured using an ABI 7900HT Fast Real Time PCR instrument (Thermo Fisher Scientific).

Transcriptomic data and analysis

TAM, CAF and endothelial Bulk RNAseq and human and mouse TAM scRNA-seq datasets were previously published and described[14,28] and datasets are publicly accessible (see 'Data Availability' section). Downstream analysis was performed using the Seurat v3 R package[80] and analysis pipeline outlined in.[14] For upstream regulator analysis we used the QIAGEN IPA (QIAGEN Inc., https://digitalinsights.qiagen.com/IPA).[36] When comparing scRNA-seq datasets between human and mouse TAMs, the Garnett package was used[81] which has previously been employed to perform mouse-human cross-species comparative analysis.[27] Murine data and a marker file specifying LYVE1 were provided to Garnett and the model was trained (train_cell_classifier()) with default

settings, using the same 2000 genes with highest variance chosen for clustering previously.[14] Publicly available human data[28] were then classified (classify_cells()) with default settings. Results were projected and plotted on the associated UMAP coordinates from the same data using a customised R script. For Illumina microarray analysis purified mRNA for the respective polarized splenocyte-derived macrophages were cultured for isolated using the PureLink® RNA Mini Kit (Invitrogen) according to the manufacturers' protocol. The purity of the isolated mRNA was assessed using a NanoDrop™ spectrophotometer (Thermo Fisher Scientific) and the quality and integrity using an Agilent 2100 Bioanalyzer (Agilent Technologies). mRNA was converted to cDNA, then subsequently amplified using the Ovation® PicoSL WTA system V2 (Tecan), biotinylated using the Encore® BiotinIL Module (Tecan), and then hybridized to MouseWG-6 V2.0 Beadchip microarray (Illumina). Following hybridization, the arrays were washed, blocked, and stained with streptavidin-Cy3 using the Whole-Genome Gene Expression Direct Hybridisation Assay (Illumina). Microarrays were run on an Illumina iScan system, raw fluorescence signals were collected using GenomeStudio (Illumina), and the data imported into Partek Genomics Suite for analysis. Background was subtracted from the raw data and fluorescence signals were normalized using the quantiles method.[89] All p-values were adjusted for multiple testing using the procedure of Benjamini and Hochberg.

QUANTIFICATION AND STATISTICAL ANALYSIS

When comparing groups for establishing statistical significance, firstly normality of the data was determined using a Shapiro-Wilk normality test and homogeneity of variance was assessed using an F-test. For normally distributed (parametric) data (where also there was also least n=6 data points in the dataset), a two-sided unpaired Students t test was conducted. A Welch's correction was applied when comparing groups with unequal variances. For non-normally distributed (non-parametric) data (or there was <6 datapoints in the dataset) a Mann-Whitney test was performed. Statistics was performed using GraphPad Prism 8 software. For microarray gene analysis, significance of differences (fold change) between the groups were assessed with Partek® Genomics Suite® software (Partek®) using an ANOVA test. Correction for multiple hypotheses was applied to p values by controlling the percentage of false discovery rate. Adjusted p values of < 0.01 were considered significant. Statistical analysis of tumor growth curves was performed using the ''CompareGrowthCurves'' function of the statmod software package.[82] The Figures legends state the cohort sizes, definitions of center (mean and median) and dispersion and precision measures (SD and SEM) and degree of significance using $^{*}p < 0.05$, $^{**}p < 0.01$, $^{***}p < 0.001$ differentiations. The text also presents mean +/- SD information for indicated cohorts. No outliers were excluded from any data presented.